Defense Threat Reduction Agency
8725 John J. Kingman Road, MS-6201
Fort Belvoir, VA 22060-6201

DTRA-TR-19-008

TECHNICAL REPORT

Estimates of Urban NUDET Organ Neutron Dose in Survivable Zone

This report is UNCLASSIFIED.

April 2019

HDTRA1-14-D-0003;0005

Prepared by:
Applied Research Associates, Inc.
801 N. Quincy Street
Suite 700
Arlington, VA 22203

This page intentionally left blank.

REPORT DOCUMENTATION PAGE	Form Approved OMB No. 0704-0188

1. REPORT DATE *(DD-MM-YYYY)*	2. REPORT TYPE	3. DATES COVERED *(From - To)*
12-04-2019	Technical Report	

4. TITLE AND SUBTITLE

Estimates of Urban NUDET Organ Neutron Dose in Survivable Zone

5a. CONTRACT NUMBER

HDTRA1-14-D-0003;0005

5b. GRANT NUMBER

5c. PROGRAM ELEMENT NUMBER

6. AUTHOR(S)

Robert Prins
Tyler Browning
Tyler Dant
Jon Cook
Kyle Millage

5d. PROJECT NUMBER

5e. TASK NUMBER

5f. WORK UNIT NUMBER

7. PERFORMING ORGANIZATION NAME(S) AND ADDRESS(ES)

Applied Research Associates, Inc.
801 N. Quincy Street, Suite 700
Arlington, VA 22203

8. PERFORMING ORGANIZATION REPORT NUMBER

9. SPONSORING/MONITORING AGENCY NAME(S) AND ADDRESS(ES)

Nuclear Technologies Department, Attn: Dr. Blake
Defense Threat Reduction Agency
8725 John J. Kingman Road, Mail Stop 6201
Fort Belvoir, VA 22060-6201

10. SPONSOR/MONITOR'S ACRONYM(S)

RD-NTS

11. SPONSOR/MONITOR'S REPORT NUMBER(S)

DTRA-TR-19-008

12. DISTRIBUTION/AVAILABILITY STATEMENT

DISTRIBUTION A. Approved for public release; distribution is unlimited.

13. SUPPLEMENTARY NOTES

14. ABSTRACT

This technical report describes computational research in which Applied Research Associates, Inc. (ARA) estimated the absorbed radiation dose to a computational phantom from incident neutron spectra in a survivable zone. The method estimates the absorbed dose to four specific organ systems; 1) spleen, 2) small intestine wall, 3) bones, and 4) lungs. The organ absorbed dose accounts for the initial neutrons and their secondary radiations. This research is important in understanding the prompt neutron dose contribution to the overall whole-body dose for personnel in the survivable zone outside of the immediate blast and thermal effects. Personnel may survive the nuclear detonation within the survivable zone and have radiation health effects that require medical assistance and resources.

15. SUBJECT TERMS

Nuclear Detonation, Medical Planning, Neutron Spectra, Computational Modeling, Absorbed Dose, HENRE, MCNP

16. SECURITY CLASSIFICATION OF:			17. LIMITATION OF ABSTRACT	18. NUMBER OF PAGES	19a. NAME OF RESPONSIBLE PERSON
a. REPORT	b. ABSTRACT	c. THIS PAGE			Paul K. Blake, PhD
U	U	U	U	45	19b. TELEPHONE NUMBER *(Include area code)* 571.616.6117

UNIT CONVERSION TABLE

U.S. customary units to and from international units of measurement*

U.S. Customary Units	Multiply by → / ← Divide by†		International Units
Length/Area/Volume			
inch (in)	2.54	$\times 10^{-2}$	meter (m)
foot (ft)	3.048	$\times 10^{-1}$	meter (m)
yard (yd)	9.144	$\times 10^{-1}$	meter (m)
mile (mi, international)	1.609 344	$\times 10^{3}$	meter (m)
mile (nmi, nautical, U.S.)	1.852	$\times 10^{3}$	meter (m)
barn (b)	1	$\times 10^{-28}$	square meter (m^2)
gallon (gal, U.S. liquid)	3.785 412	$\times 10^{-3}$	cubic meter (m^3)
cubic foot (ft^3)	2.831 685	$\times 10^{-2}$	cubic meter (m^3)
Mass/Density			
pound (lb)	4.535 924	$\times 10^{-1}$	kilogram (kg)
atomic mass unit (AMU)	1.660 539	$\times 10^{-27}$	kilogram (kg)
pound-mass per cubic foot ($lb\ ft^{-3}$)	1.601 846	$\times 10^{1}$	kilogram per cubic meter ($kg\ m^{-3}$)
Pound-force (lbf avoirdupois)	4.448 222		Newton (N)
Energy/Work/Power			
electron volt (eV)	1.602 177	$\times 10^{-19}$	joule (J)
erg	1	$\times 10^{-7}$	joule (J)
kiloton (kT) (TNT equivalent)	4.184	$\times 10^{12}$	joule (J)
British thermal unit (Btu) (thermochemical)	1.054 350	$\times 10^{3}$	joule (J)
foot-pound-force (ft lbf)	1.355 818		joule (J)
calorie (cal) (thermochemical)	4.184		joule (J)
Pressure			
atmosphere (atm)	1.013 250	$\times 10^{5}$	pascal (Pa)
pound force per square inch (psi)	6.984 757	$\times 10^{3}$	pascal (Pa)
Temperature			
degree Fahrenheit (°F)	[T(°F) − 32]/1.8		degree Celsius (°C)
degree Fahrenheit (°F)	[T(°F) + 459.67]/1.8		kelvin (K)
Radiation			
activity of radionuclides [curie (Ci)]	3.7	$\times 10^{10}$	per second (s^{-1}‡)
air exposure [roentgen (R)]	2.579 760	$\times 10^{-4}$	coulomb per kilogram ($C\ kg^{-1}$)
absorbed dose (rad)	1	$\times 10^{-2}$	joule per kilogram ($J\ kg^{-1}$§)
equivalent and effective dose (rem)	1	$\times 10^{-2}$	joule per kilogram ($J\ kg^{-1}$**)

*Specific details regarding the implementation of SI units may be viewed at http://www.bipm.org/en/si/.

†Multiply the U.S. customary unit by the factor to get the international unit. Divide the international unit by the factor to get the U.S. customary unit.

‡The special name for the SI unit of the activity of a radionuclide is the becquerel (Bq). ($1\ Bq = 1\ s^{-1}$).

§The special name for the SI unit of absorbed dose is the gray (Gy). ($1\ Gy = 1\ J\ kg^{-1}$).

**The special name for the SI unit of equivalent and effective dose is the sievert (Sv). ($1\ Sv = 1\ J\ kg^{-1}$).

Table of Contents

List of Figures

List of Tables

Acknowledgements

The authors would like to express our appreciation to the experimentalists involved with conducting the research and producing the data evaluated in this report. We would like to recognize the efforts of Dr. Daniela Stricklin (Department of Energy), Dr. Kevin Kramer (Lawrence Livermore National Laboratory) in providing a technical review of the report. Their contributions to the discussions leading to the progress presented here and peer feedback of our findings were invaluable. We also gratefully acknowledge Dr. Paul Blake of DTRA/RD-NTS for programmatic support. This work was performed under DTRA contract HDTRA1-14-D-0003;0005.

Executive Summary

Current methods for estimating radiation casualties from a nuclear detonation (NUDET) combine neutron and gamma exposure into a single whole-body radiation dose. As a result, there is minimal accounting for how the different types of radiation interact within the human body and how the radiation dose may differ among the critical organ structures. Traditional methods have focused on the radiation dose from gammas, and little research has been conducted looking into the contribution of dose from the incident neutron spectrum. The purpose of this study is to investigate the neutron energy deposition in four specific organs within a computational phantom from a neutron spectrum in potential survivable zones immediately following a nuclear detonation.

Applied Research Associates, Inc. (ARA) previously published research investigating the neutron energy spectra emitted from NUDETs (Kramer, 2018). Prior assumptions to Kramer's research were that the neutron dose would be vastly overwhelmed by the gamma dose contribution at that location and subsequently any person surviving the detonation. Kramer's research showed that the neutron contribution to health effects depends on scenario specific details and that personnel in the survivable areas surrounding a nuclear detonation would receive a non-negligible radiation free-in-air dose from neutrons.

This current research takes the next step and uses the propagated survivable zone neutron spectra from two publically releasable neutron source spectra (fission-type weapon and low-yield thermonuclear weapon) as an incident spectra on an adult computational phantom (Korean Typical MAN-2 (ORNL, 2019)) to determine the neutron energy deposition in four organs of interest. For both spectra, the highest organ absorbed dose per neutron yield at the survivable range was determined to be the small intestine wall with the source spectrum incident on the anterior side of the computational phantom. The lowest overall absorbed dose (to the specific organs) for both spectra occurred when the source spectrum was incident on the left lateral side of the computational phantom. Understanding the radiation absorbed dose from the neutron source spectrum will further assist researchers in minimizing the amount of uncertainties involved in assigning whole-body radiation dose estimates to personnel located at the survivable range from a NUDET.

Section 1. Background

There are three sources of neutrons following a NUDET. Prompt neutrons (from the fission or fusion reactions in the weapon source material) are produced as part of the chain-reaction creating the detonation and result from the interactions within the nuclear source material. Delayed neutrons arise from the decay of the fission products during the first minute following the detonation. The third source of neutrons, those produced in the interaction of the high-energy gamma radiation with the weapon material and detonation environment is negligible with respect to the prompt and delayed neutrons, and will not be addressed.

The three basic nuclear weapon types include fission, fusion, and small modified thermonuclear (enhanced radiation weapon). For fission-type weapons, neutrons are produced in the fissionable source material when the unstable nuclear bonds of the nucleus receive enough energy (in the form of an initial neutron) to split, releasing additional neutrons and energy. The fusing of hydrogen isotopes (deuterium and tritium) and other heavier nuclei are the source of the neutrons released in a fusion-type weapon. Fusion neutron energies are about ten times higher than the typical energies of a fission neutron. Enhanced radiation weapon (small modified thermonuclear) are designed to release neutrons around one order of magnitude greater than that of a standard fission-type weapon of similar yield. Many nuclear weapons have both fission and fusion components which further complicates an already diverse spectra of energies (Kramer, Dant, Li, & Millage, 2017). As prompt fusion neutrons can have energies up to 14 MeV and prompt fission neutrons can have energies higher than 2 MeV, the combination of high neutron yield with higher energies can lead to larger neutron radiation absorbed doses over a greater distance from ground zero (Mickelson, 2012).

In general, the ratio of the prompt to delayed neutrons escaping the immediate weapon environment is 20:1 (Project, 1953). The overall number of neutrons emitted depends on the weapon's design and yield. For example, the nuclear artillery shell design allowed a larger number of neutrons to escape the weapon components than a more conventional nuclear device design due to fewer absorbing materials surrounding the fissionable material. In a conventional design, there are more materials of low atomic number in the weapon components, which absorb the neutrons at a higher rate. In this manner, each nuclear weapon has a characteristic neutron spectrum made up of the total number of neutrons per energy bin emitted per kiloton of yield (Carter, Bond, Veenstra, Reed, & Silvia, 1953)

Neutrons emitted from the detonation propagate in an approximate isotropic fashion from the vertex. The total neutron flux, neutron flux density, and average neutron energy decreases as the distance from ground zero increases. This reduction effect is due to 1) geometrical dispersion due to the Inverse Square Law, 2) atmospheric attenuation and neutron capture as the neutrons move through air and water vapor present in the environment, 3) neutron nucleus elastic scattering in the environment, and 4) spontaneous free neutron beta decay during transit to the biological location of interest. Therefore the total neutron flux that interacts with a target includes both the scattered neutrons and the direct neutrons which do not undergo any interaction between the source and the target. As a result, the neutron flux at that target is a location-dependent spectrum of energies. There is also a time-dependent spectral shift of the neutron arrival as the unscattered fast neutrons will arrive first followed by the more thermalized and scattered neutrons. This time-dependent spectral shift of the neutron arrival is not considered as biologically interesting as the neutron energy spectrum and will not be discussed in this technical report (Bond, Carter, Reed, Hechter, & Veenstra, 1953).

Neutron interactions in a medium (e.g. atmosphere or tissue) may be conveniently classified as either elastic scattering, inelastic scattering, or absorption events. An elastic scattering event is any interaction where a neutron exchanges a virtual gauge boson with a nearby nucleus and therefore gives that nucleus a share of its momentum and energy, but it does not change the quantum state of that nucleus (i.e. "n-n reactions"). An inelastic scattering event is any interaction where the neutron exchanges a virtual gauge boson with a nearby nucleus, and as a result that nucleus enters an excited quantum state (and may therefore subsequently fission, re-emit gamma radiation, eject a proton, etc.). An absorption event is a type of inelastic scattering where the neutron and associated kinetic energy is entirely absorbed by a nucleus. Note that gamma radiation is not emitted directly by the target nucleus during or after an elastic scattering event, but inelastic and absorption events may (and often does) involve direct gamma re-emission. Accounting for the different types of neutron interactions is important since neutrons interacting with the human body may undergo numerous elastic scattering events prior to an inelastic scattering or absorption event.

Uncharged neutrons are indirectly ionizing radiation, depositing their energy via secondary radiations which come about by scattering and capture reactions. Neutrons will interact directly with the atomic nucleus and eject fast recoil protons, alpha particles, and heavier nuclear fragments, which will go on to interact with cellular DNA. X- and gamma-rays will interact with orbital electrons rather than the atomic nucleus.

Neutrons in the survivable regions outside of ground zero will have a spectrum of energies conventionally divided into three regions: thermal (< 1 eV), epithermal (approximately 1 eV up to 10 keV), and fast (>10 keV up to MeV) (Attix, 1986). Neutrons in the fast energy region will primarily undergo repeated scattering in an environment and eventually be reduced to thermal energies. Thermal energy cross sections, probability per unit path length of the neutron interacting with the medium through which it is traversing, are much greater than fast neutron cross sections. This trend is particularly true for low atomic-number elements, which predominantly make up the human body.

The low atomic-number elements that dominate in the human body are hydrogen (H), nitrogen (N), oxygen (O), and carbon (C). These four elements each have only one primary natural isotope, with other isotopes being quite rare on Earth and therefore also rare in the human body. These isotopes generally have high interaction cross sections at neutron energies below 1 MeV (Figure 1). Furthermore each isotope's total interaction cross section is different, therefore a 1-MeV neutron interacting with different tissues each composed of different elemental compositions, will have different probabilities of interaction. In the thermal neutron energy range (0.5 eV or 5.0×10^{-7} MeV) and below, hydrogen and nitrogen have the highest probability of interaction. In the intermediate neutron energy range (5.0×10^{-7} MeV up to 1.0×10^{-2} MeV), hydrogen and nitrogen still have the highest probability of interaction with a neutron. Neutrons will have a similar probability of interaction with the four elements in the fast neutron energy range above 1.0×10^{-2} MeV.

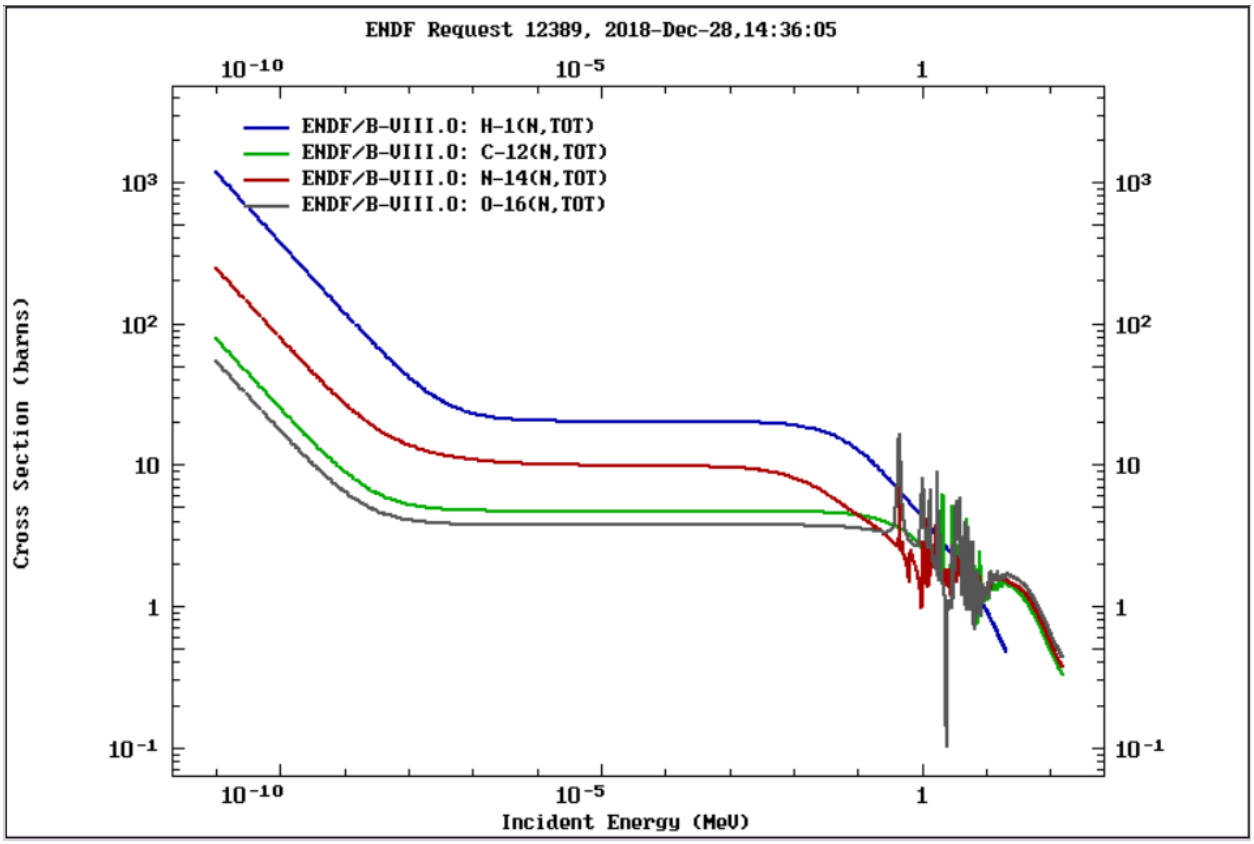

Figure 1. Evaluated Nuclear Data File (ENDF) plot for the total interaction neutron cross section with ^{1}H, ^{14}N, ^{16}O, and ^{12}C (Cross Section Evaluation Working Group, 2018).

As described above, neutrons in the thermal range up through the fast energy range will have the highest probability of interaction with hydrogen and nitrogen. There are three reactions that can occur when a neutron interacts with these two elements: 1) nitrogen capture, $^{14}N(n,p)^{14}C$, where a proton is ejected, 2) hydrogen capture, $^{1}H(n,\gamma)^{2}H$, accompanied by the ejection of a photon, and 3) neutron scattering by hydrogen with a subsequent production of recoil protons.

The nitrogen capture cross section is $\sigma_N = 0.226E^{-1/2}$ barns (E is the energy of the incident neutron in eV) with the ejected proton having an approximate energy of 580 keV plus the energy of the incident neutron. Since all nonrelativistic (less than about 1 MeV) protons will lose energy due to electromagnetic interactions at a rate on the order of 500 MeV per cm, protons in the non-relativistic regime will have a short (roughly 30 micrometers) mean free path (Appendix A). The hydrogen capture cross section is $\sigma_H = 0.049E^{-1/2}$ barns, with the ejected photon having an approximate energy of 2.2 MeV. The energy liberated per neutron when scattered by hydrogen is approximately one-half of the energy of the incident neutron (Armed Forces Special Weapons Project, 1953).

Neutrons and associated energies above 1 MeV will primarily experience elastic scattering events and as they decrease in energy, the probability of inelastic scattering and capture increases. Therefore, neutron energies below 1 MeV will have a higher likelihood of multiple nitrogen and hydrogen capture events. For neutrons below 0.2 MeV, the contribution of the proton recoil reaction to the total energy released from the neutron is increased (Figure 2). At neutron energies in the thermal and epithermal range, secondary photons from hydrogen capture account for 90%

of the radiation absorbed dose in the body as the photons deposit their energy via secondary radiations (electrons and positrons). The rest of the radiation absorbed dose originates from the nitrogen capture reaction. At neutrons energies greater than the epithermal range, the absorbed dose from photons is less than 20% (ICRP, 2010).

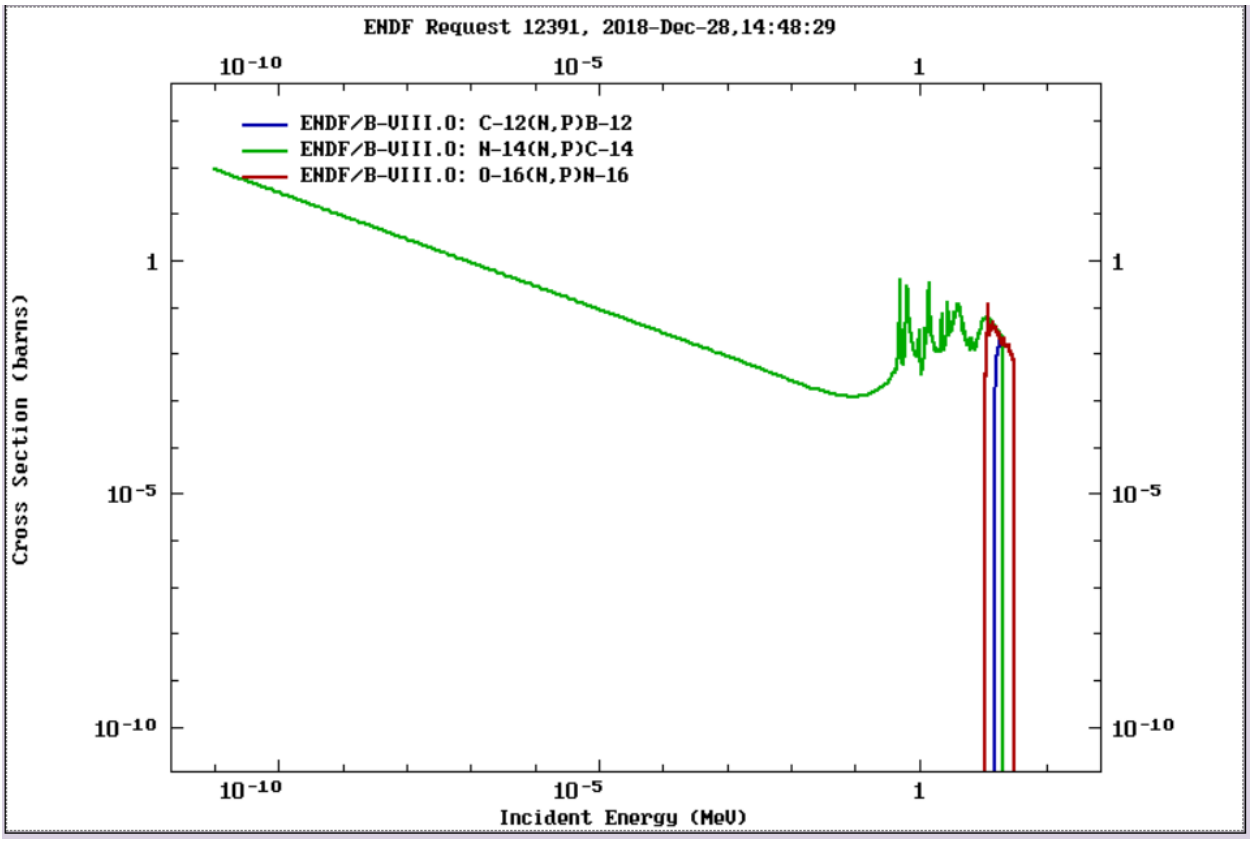

Figure 2. ENDF plot of the neutron cross section reaction leading to recoil protons for 14N, 12C, and 16O (Cross Section Evaluation Working Group, 2018).

When a target is bombarded by billions of neutrons across a spectrum of energies from a NUDET, individual calculations of where a neutron will interact, what type of interaction ensues, what type of secondary radiation is produced, and how the energy is deposited becomes impossible without the use of probabilistic transport codes and computational phantoms. Computational phantoms are commonly used to ascertain the effects of radiation interaction within the human body. Each major portion of the body is segmented and given a material composition similar to reality. Material composition standards for many materials and environments can be found in the Compendium of Material Composition Data for Radiation Transport Modeling from Pacific Northwest National Laboratory (McConn Jr., Gesh, Pagh, Rucker, & Williams III, 2011). The elemental composition differs with respect to the organs in the body.

Table 1 provides an example of the organ composition difference with data extracted from ICRP Report 110, Adult Reference Computational Phantoms (ICRP, 2009).

Table 1. Portion extracted from ICRP 110 Table B.1. List of media, their elemental compositions (percentages by mass), and their densities for the adult male reference computational phantom.

Organ	^{1}H	^{6}C	^{7}N	^{8}O	^{11}Na	^{12}Mg	^{15}P	^{16}S	^{17}Cl	^{19}K	^{20}Ca	Density (g/cm^{3})
Small Intestine	10.5	11.3	2.6	75.0	0.1	-	0.1	0.1	0.2	0.1	-	1.040
Lung Tissue	10.3	10.7	3.2	74.6	0.2	-	0.2	0.3	0.3	0.2	-	0.382
Spleen	10.2	11.1	3.3	74.3	0.1	-	0.2	0.2	0.3	0.2	-	1.040
Cortical Bone	3.6	15.9	4.2	44.8	0.3	0.2	9.4	0.3	-	-	21.3	1.904
Humeri and Femora upper halves, medullary cavity	11.5	63.6	0.7	23.9	0.1	-	-	0.1	0.1	-	-	0.980
Pelvis, spongiosa	9.4	36.0	2.5	45.4	0.2	-	2.1	0.3	0.2	0.1	3.8	1.123
Ribs, spongiosa	8.9	29.2	2.9	50.7	0.2	-	2.6	0.4	0.2	0.1	4.8	1.165

Section 2. Methodology

We used previously propagated ideal neutron source spectra in an urban environment and determined a distance away from ground zero where the reduced neutron spectra convolved with ICRP-116 Male Red Marrow ISO flux-to-dose conversion factors to determine survivable location zones (Kramer, 2018). The transition threshold from the severe radiation injury zone to the moderate radiation injury zone is 2.9 Gy, representing the bone marrow $LD_{50/60}$ dose estimate. An additional transition threshold from the moderate radiation injury zone to the light radiation injury zone is 0.5 Gy. Deterministic radiation health effects are asymptomatic below 0.25 Gy. As Kramer noted, "In the case of a surface burst, and especially in the case of an urban emplaced improvised nuclear device (IND), the weapon effects will be attenuated and potentially-treatable victims are likely to be much closer to the detonation, as a result, they may be exposed to prompt neutrons as part of their total radiation dose." Similarly, "the percentage of absorbed dose from prompt neutrons in the moderate radiation injury zone can increase from 13% of the total prompt absorbed dose in the open, to as much as 43% of the total dose in the urban scenario" (Kramer, 2018).

Two source spectra were used in this study, a fission-type spectra similar to the Little Boy weapon used in Hiroshima (Young & Kerr, 2005) and a representative low-yield thermonuclear weapon spectrum (Auxier, et al., 1972). Figure 3 shows the propagated spectra within dry air in the urban geometry in the potential survivable zone.

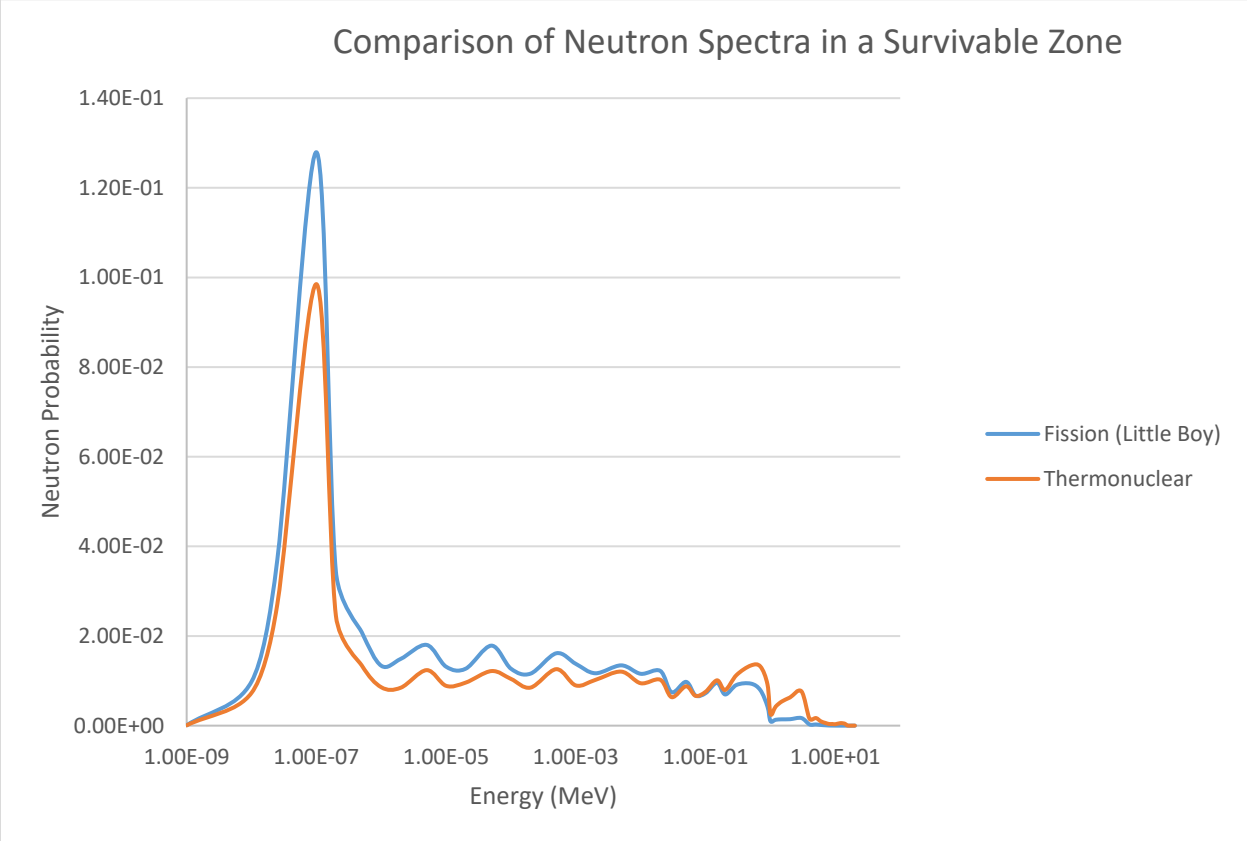

Figure 3. Neutron spectra in the survivable zone from both the fission-type and low-yield thermonuclear weapon.

Kramer's research normalized each of the source spectra to a 10 kT yield and examined the impact that urban terrain has on the shielding and attenuation of prompt radiation as compared to a similar event in an open field (Kramer, 2018). Kramer showed that the potentially survivable radiation injury zone were from 550 m to about 800 m and 650 m to about 1,000 m for the Little Boy and Low Yield source term respectively. Our research used the two extracted neutron spectra, as propagated to the potentially survivable zone (moderate radiation injury zone) in the simulated urban environment (Figure 4 and Figure 5), as a planar neutron source within the MCNP radiation transport code (MCNP6.2) incident on the computational phantom (Kramer, 2018).

MCNP is a general-purpose Monte Carlo N-Particle code used to understand the energy deposition from neutron, photon, electron, or coupled neutron/photon/electron transport (Werner, 2017). For each neutron spectrum, the simulation was divided into two parts: >1 MeV, and <1 MeV. The reason for this division is the relatively short mean free path of <1 MeV protons discussed previously. In fact, this mean free path is so short that it cannot be meaningfully propagated in the computational phantom. Due to limitations of MCNP6.2, proton transport cannot be performed in a parallel computing environment. Although protons will contribute in a nontrivial manner to the dose received, it is very computationally resource intensive to perform proton propagation in the model. We circumvent this limitation by dividing the simulation into two parts: one with no proton transport at low initial neutron energy and exploiting parallel computing architectures, and another with proton transport at high initial neutron energy using only serial computing. We then take the weighted sum (<1 MeV is roughly 72% of the total initial neutron spectrum for both the Little Boy and Thermonuclear spectra) of the two results to estimate the total dose received.

In the low energy (<1 MeV) simulations, more than 500 million particle histories were used to minimize the statistical error in the results. The high energy simulations used 50 million (Little Boy) and 39 million (Thermonuclear) histories. The neutron energy distribution and associated uncertainties increase for low energy neutrons in the moderate radiation injury zone with respect to ground zero (Figure 4 and Figure 5) (Kramer, 2018). This is a result of the indirect relationship of the interaction probabilities of the elements in the air and the neutron energy.

The intervening environment presents a major contribution to shaping the incident neutron spectrum. For example, the humidity in the air, bodies of water, and concrete can potentially present large quantities of hydrogen that moderate the high-energy neutrons down to more damaging thermal energies. In addition to line-of-sight materials, other materials surrounding the target affect the neutron spectrum. For these reasons, the survivable energy spectra given in this report are not "the" survivable spectra but rather an example of two possible realistic spectra in the survivable zone. We present the data as dose per incident neutron; where 'incident neutron' in this case is the number of neutrons emitted from a 2.25 × 2.25 meter square planar surface roughly one meter away from the computational phantom. The neutrons are normalized by the ratio of the solid angle swept by our planar source on a 1.5 km sphere centered on the detonation vertex (in steradians) by 4π steradians (the solid angle of a sphere). Therefore, we note that the resulting calculations are – for reasons previously discussed – decoupled from the explosive yield, environmental particularities, and design of any specific weapon. All results are general representative examples of the dose received by an average man in an urban environment, but not necessarily applicable to any specific physical scenario.

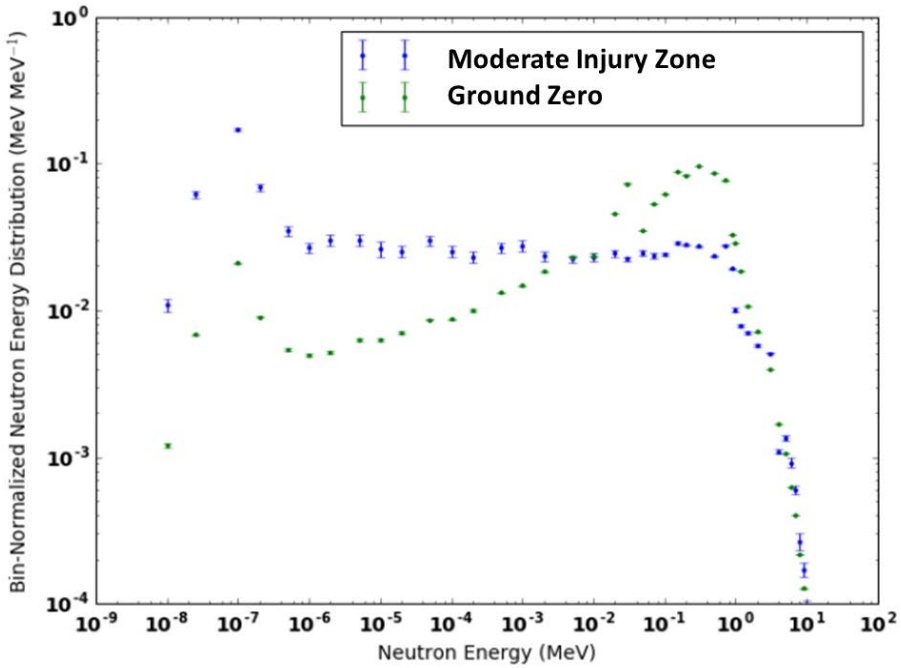

Figure 4. Neutron energy spectra plot in 42 bins weighted by neutron energy and normalized by the width of the bin for the Little Boy source. The potentially survivable radiation injury zone occurs approximately 600 m from ground zero in an urban environment (Kramer, 2018).

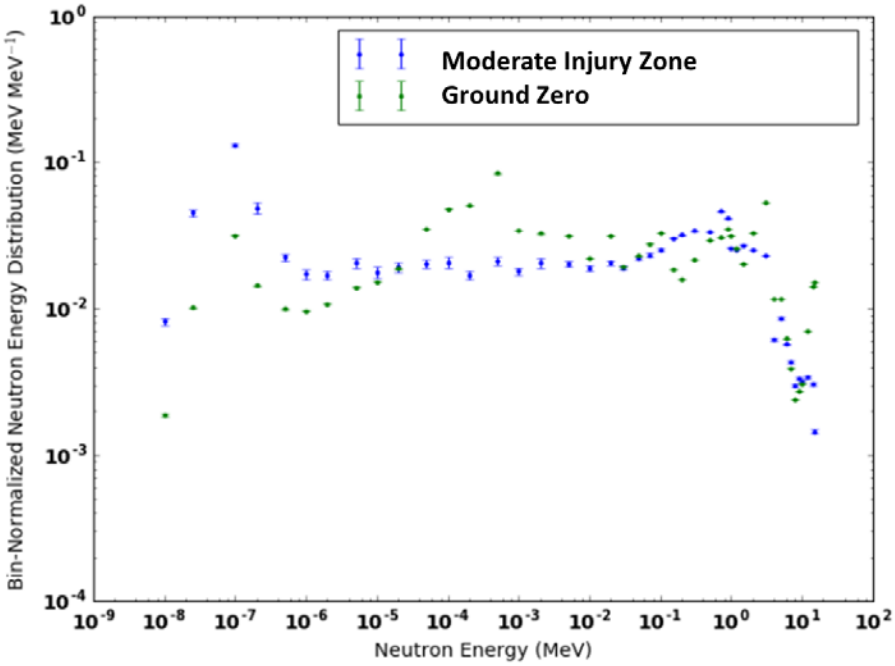

Figure 5. Neutron energy spectra plot in 42 bins weighted by neutron energy and normalized by the width of the bin for the 'Low Yield Thermonuclear' source. The potentially survivable radiation injury zone occurs approximately 900 m from ground zero in an urban scenario (Kramer, 2018).

For our research we were primarily interested in the energy deposition of neutrons and neutron-induced photons within a phantom. The computational phantom used in this study is available from the Radiation Safety Information Computational Center (RSICC) at Oak Ridge National Laboratory. The computational phantom is Korean Typical MAN-2 (KTMan-2) distributed with the MCNPX software package (Pelowitz, 2011) from RSICC (ORNL, Radiation Safety Information Computational Center, 2019) and was funded by the Korean Ministry of Science and Technology (Figure 6). The phantom has a voxel array size of 300 × 150 × 344 where each voxel has dimensions of 2mm × 2mm × 5mm. The KTMan-2 phantom was developed in January 2004 with further modifications applied in April 2006. Computational phantoms are commonly used in the medical and radiation-protection dosimetry industry. The phantom is segmented with 19 different materials: adipose tissue, soft tissue (male), brain (whole), gastrointestinal tract, heart (blood-filled), kidney, liver, lung (healthy and inflated), skeletal muscle, pancreas, cartilage, skin, spleen, testes, thyroid, urinary bladder (urine-filled), water, bone mixture, and air (dry, near sea level).

Figure 6. KTMan-2 computational phantom represented in MCNP6.2.

For the purposes of this research, we studied four different organ systems: 1) spleen, 2) small intestine wall, 3) lungs, and 4) skeletal bones. Although not vital to survival, we studied the spleen because of its importance to the immune system. The spleen produces white blood cells that help to fight infection. The spleen also helps other organs (i.e. liver) remove damaged red blood cells (Mandal MD, 2019). The small intestine is the primary location for nutrients and minerals from food to be absorbed into the blood stream. The absorption occurs through the inner surface area of the small intestine wall (Mandal MD, 2019). We are also interested in the radiation absorbed dose to the lung because of radiation pneumonitis. Radiation pneumonitis is an inflammation of the lung that primarily occurs as a result of radiation therapy with similar symptoms to pneumonia.

Severe pneumonitis can persist for months following the radiation treatment and can lead to permanent scarring. The body's response to the inflammation is the release of white blood cells (Eldridge MD, An Overview of Radiation Pneumonitis, 2019).

Finally, we are interested in understanding the amount of radiation absorbed dose to the bone marrow in the body. Red bone marrow is primarily found in the flat bones of the body; hip bone, breast bone, and ribs (among others) and are also found in the proximal ends of the femur and humerus (ScienceDaily, 2019). White blood cells are created in the bone marrow via a process called hematopoiesis. Although all blood cells originate from hematopoietic stem cells, the differentiation of the stem cells eventually results in the white blood cells that are very important in fighting any infection in the body (Eldridge MD, 2019). For this research, we were unable to tally the radiation dose in the computational phantom for the bone marrow. Therefore the estimate of the absorbed radiation dose to the bone is more specifically all the skeletal bones in the body rather than just the flat bones.

The research question to be answered is how the neutron spectrum deposits energy in specific organs at a survivable range from a NUDET within a computational phantom and whether the energy deposition is directionally dependent.

To best account for environmental scattering conditions, we modeled the computational phantom on a soil disc (Figure 7). The soil disc is composed of typical Western U.S. soil and the air in between the source spectrum and the computational phantom is dry air (McConn Jr, Gesh, Pagh, Rucker, & Williams III, 2011) (ORNL, Radiation Safety Information Computational Center, 2019).

Table 2. MCNP material card for soil and air (McConn Jr, Gesh, Pagh, Rucker, & Williams III, 2011).

Elemental Composition (element/isotope identifier with library identification)	Atomic Fraction of the Isotope in the Material
Soil (Earth, Typical Western U.S.)	
1001.70c	0.316855
8016.70c	0.501581
13027.70c	0.039951
14000.60c	0.141613
Dry Air	
6000.70c	0.0124
7014.70c	75.5267
8016.70c	23.1781
18000.42c	1.2827

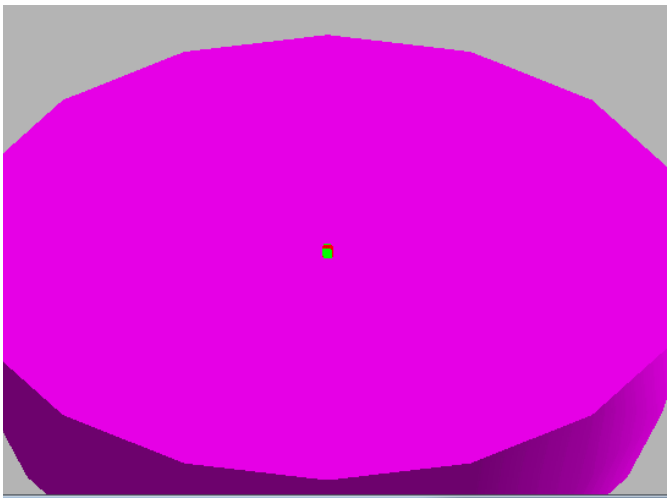

Figure 7. Modeled soil disc (purple) with the computational phantom centrally positioned (green/red) to best account for the neutron scattering off of the ground.

We used the material card inputs for the target organs that came with the computational phantom. The Departments of Homeland Security and Energy published additional material composition data, which can also be used in radiation transport modeling input decks (McConn Jr, Gesh, Pagh, Rucker, & Williams III, 2011).

Table 3. MCNP Material Card for Target Organs.

Elemental Composition (element/isotope identifier with library identification) (ORNL, Radiation Safety Information Computational Center, 2019)	Atomic Weight Fraction of Isotope in the Material
Bone Mixture (ORNL8381 report)	
1001.70c	0.07337
6000.70c	0.25475
7014.70c	0.03057
8016.70c	0.47893
9019.70c	0.00025
11023.70c	0.00326
12000.60c	0.00112
14000.60c	0.00002
15031.70c	0.05095
16000.61c	0.00173
17000.60c	0.00143
19000.60c	0.00153
20000.60c	0.10190
26000.50c	0.00008
30000.70c	0.00005
37087.70c	0.00002
38088.70c	0.00003
82000.50c	0.00001
Spleen	
1001.70c	0.103

6000.70c	0.113
7014.70c	0.032
8016.70c	0.741
11023.70c	0.001
15031.70c	0.003
16000.61c	0.002
17000.60c	0.002
19000.60c	0.003
Lung (healthy and inflated)	
1001.70c	0.103
6000.70c	0.105
7014.70c	0.031
8016.70c	0.749
11023.70c	0.002
15031.70c	0.002
16000.61c	0.003
17000.60c	0.003
19000.60c	0.002
GI Tract	
1001.70c	0.106
6000.70c	0.115
7014.70c	0.022
8016.70c	0.751
11023.70c	0.001
15031.70c	0.001
16000.61c	0.001
17000.60c	0.002
19000.60c	0.001

The survivable neutron spectrum was incident on the phantom at a 10° offset from normal (Figure 8). This was done to account for how the neutrons might be incident on a person with respect to the emission of the neutrons.

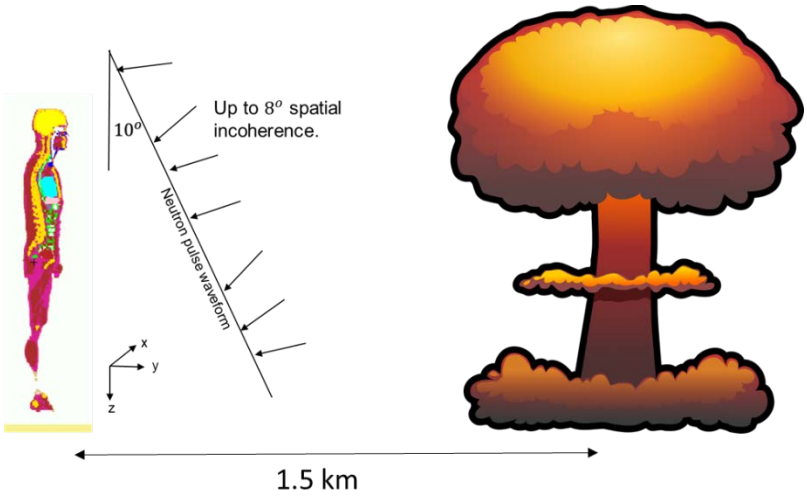

Figure 8. Simulated layout of the phantom with respect to the incident neutron spectrum which was propagated in an urban environment.

Two neutron spectra were incident on a computational phantom standing on soil from four different angles apiece. For each spectrum, the energy deposited by the initial neutrons and secondary radiations was tallied in MCNP6.2. We reduced the statistical error by using 500 million histories for the low energy simulations. The low energy simulations were run on DoD high performance computing platforms as an effort to reduce the computational expense. The high energy simulation with proton propagation was performed in a single process computational environment on an ARA personal computer. Finally, although all the radiation dose received by an organ of interest in this simulation is from an incident neutron (the 'grandparent' particle), we assume that the likelihood of the grandparent particle ionizing organ tissues is low. Instead, it is instructive to divide this dose up by the final daughter particle species prior to the particle being captured and depositing its energy. In this manner, we were able to understand what specific interaction mechanism are responsible for the tissue damage.

Section 3. Results

We present the low-yield thermonuclear and fission (Little Boy) spectra results in Table 4-7. The greatest amount of statistical error in the four organs was observed in the spleen. This was to be expected as the spleen is a relatively small geometrically-shaped organ. The statistical error is a measurement of the precision not the accuracy of the absorbed dose.

Table 4. Initial low-yield thermonuclear (TN) and Little Boy (LB) spectra propagated in an urban environment incident on a computational phantom from the left lateral direction with respect to the computational phantom.

Radiation Type	Source spectra incident on the phantom from the left lateral direction; absorbed dose per radiation type (mGy/neutron)							
	Lung (statistical error)		Bone (statistical error)		Small Intestine Wall (statistical error)		Spleen (statistical error)	
	TN	LB	TN	LB	TN	LB	TN	LB
Neutron	4.20E-21 (0.37%)	4.20E-21 (0.30%)	8.76E-21 (0.07%)	8.84E-21 (0.07%)	6.17E-21 (0.52%)	6.17E-21 (0.51%)	9.67E-22 (1.33%)	9.76E-22 (1.27%)
Gamma	2.41E-21 (0.24%)	2.71E-21 (0.22%)	3.02E-21 (0.11%)	3.45E-21 (0.10%)	2.79E-21 (0.30%)	3.13E-21 (0.28%)	1.57E-21 (0.80%)	1.75E-21 (0.76%)
Beta	2.37E-21 (0.65%)	2.67E-21 (0.60%)	2.93E-21 (0.20%)	3.33E-21 (0.19%)	2.74E-21 (0.69%)	3.02E-21 (0.64%)	1.51E-21 (2.05%)	1.77E-21 (1.89%)
Proton	5.71E-21 (1.63%)	5.58E-21 (1.44%)	1.20E-20 (0.33%)	1.18E-20 (0.30%)	9.19E-21 (1.60%)	9.09E-21 (1.41%)	1.39E-21 (8.68%)	1.23E-21 (8.09%)
Total	1.47E-20 (1.81%)	1.52E-20 (1.60%)	2.67E-20 (0.41%)	2.75E-20 (0.37%)	2.09E-20 (1.85%)	2.14E-20 (1.66%)	5.43E-21 (9.05%)	5.73E-21 (8.44%)

Table 5. Initial low-yield thermonuclear (TN) and Little Boy spectra propagated in an urban environment incident on a computational phantom from the right lateral direction with respect to the computational phantom.

Radiation Type	Source spectra incident on the phantom from the right lateral direction; absorbed dose per radiation type (mGy/neutron)							
	Lung (statistical error)		Bone (statistical error)		Small Intestine Wall (statistical error)		Spleen (statistical error)	
	TN	LB	TN	LB	TN	LB	TN	LB
Neutron	4.65E-21 (0.28%)	4.62E-21 (0.27%)	8.83E-21 (0.07%)	8.79E-21 (0.07%)	8.37E-21 (0.41%)	8.29E-21 (0.41%)	7.76E-21 (0.56%)	7.66E-21 (0.54%)
Gamma	2.83E-21 (0.24%)	2.82E-21 (0.22%)	3.41E-21 (0.11%)	3.41E-21 (0.10%)	3.78E-21 (0.28%)	3.78E-21 (0.26%)	4.79E-21 (0.51%)	4.84E-21 (0.47%)
Beta	2.78E-21 (0.64%)	2.79E-21 (0.59%)	3.31E-21 (0.20%)	3.31E-21 (0.19%)	3.71E-21 (0.64%)	3.68E-21 (0.59%)	4.72E-21 (1.28%)	4.67E-21 (1.19%)
Proton	6.41E-21 (1.52%)	6.24E-21 (1.36%)	1.19E-20 (0.33%)	1.18E-20 (0.30%)	1.26E-20 (1.37%)	1.23E-20 (1.22%)	1.02E-20 (3.05%)	1.01E-20 (2.70%)
Total	1.67E-21 (1.69%)	1.65E-20 (1.52%)	2.74E-20 (0.41%)	2.73E-20 (0.37%)	2.84E-20 (1.59%)	2.80E-20 (1.44%)	2.75E-20 (3.39%)	2.73E-20 (3.04%)

Table 6. Initial low-yield thermonuclear (TN) and Little Boy (LB) spectra propagated in an urban environment incident on a computational phantom from the anterior to posterior direction with respect to the computational phantom.

Radiation Type	Source spectra incident on the phantom from the anterior to posterior direction; absorbed dose per radiation type (mGy/neutron)							
	Lung (statistical error)		Bone (statistical error)		Small Intestine Wall (statistical error)		Spleen (statistical error)	
	TN	LB	TN	LB	TN	LB	TN	LB
Neutron	1.81E-20 (0.87%)	1.80E-20 (0.16%)	1.48E-20 (0.06%)	1.47E-20 (0.06%)	2.30E-20 (0.18%)	2.29E-20 (0.18%)	1.14E-20 (0.57%)	1.14E-20 (0.55%)
Gamma	7.71E-21 (0.15%)	7.73E-21 (0.14%)	6.58E-21 (0.08%)	6.59E-21 (0.07%)	1.08E-20 (0.17%)	1.09E-20 (0.16%)	7.78E-21 (0.40%)	7.83E-21 (0.37%)
Beta	7.52E-21 (0.40%)	7.59E-21 (0.37%)	6.39E-21 (0.14%)	6.39E-21 (0.13%)	1.05E-20 (0.39%)	1.05E-20 (0.36%)	7.79E-21 (0.98%)	7.68E-21 (0.94%)
Proton	2.51E-20 (0.74%)	2.48E-20 (0.66%)	1.96E-20 (0.26%)	1.94E-20 (0.23%)	3.13E-20 (0.83%)	3.09E-20 (0.73%)	1.58E-20 (2.45%)	1.53E-20 (2.19%)
Total	5.84E-20 (0.87%)	5.81E-20 (0.78%)	4.73E-20 (0.31%)	4.71E-20 (0.28%)	7.57E-20 (0.95%)	7.52E-20 (0.85%)	4.28E-20 (2.73%)	4.22E-20 (2.47%)

Table 7. Initial low-yield thermonuclear (TN) and Little Boy (LB) spectra propagated in an urban environment incident on a computational phantom from the posterior to anterior direction with respect to the computational phantom.

Radiation Type	Source spectra incident on the phantom from the posterior to anterior direction; absorbed dose per radiation type (mGy/neutron)							
	Lung (statistical error)		Bone (statistical error)		Small Intestine Wall (statistical error)		Spleen (statistical error)	
	TN	LB	TN	LB	TN	LB	TN	LB
Neutron	1.92E-20 (0.12%)	1.95E-20 (0.15%)	1.34E-20 (0.05%)	1.33E-20 (0.06%)	6.26E-21 (0.28%)	6.21E-21 (0.36%)	1.73E-20 (0.36%)	1.71E-20 (0.45%)
Gamma	7.94E-21 (0.13%)	7.98E-21 (0.13%)	6.72E-21 (0.07%)	6.73E-21 (0.07%)	6.92E-21 (0.18%)	6.92E-21 (0.18%)	9.51E-21 (0.34%)	9.50E-21 (0.35%)
Beta	7.73E-21 (0.36%)	7.75E-21 (0.36%)	6.55E-21 (0.13%)	6.56E-21 (0.13%)	6.89E-21 (0.40%)	6.85E-21 (0.43%)	9.39E-21 (0.84%)	9.26E-21 (0.86%)
Proton	2.74E-20 (0.71%)	2.68E-20 (0.63%)	1.77E-20 (0.27%)	1.74E-20 (0.24%)	9.07E-21 (1.62%)	8.89E-21 (1.44%)	2.33E-20 (1.98%)	2.27E-20 (1.77%)
Total	6.26E-20 (0.82%)	6.21E-20 (0.76%)	4.43E-20 (0.31%)	4.40E-20 (0.29%)	2.91E-20 (1.70%)	2.89E-20 (1.56%)	5.95E-20 (2.21%)	5.86E-20 (2.05%)

The highest amount of absorbed dose to the small intestine wall occurred when neutron spectrum was incident on the anterior-posterior side of the computational phantom. Interestingly, the lung and spleen dose was highest when the spectrum on the computational phantom was incident on the posterior. The smallest amount of overall absorbed dose to the four organs occurred when the neutron spectrum was incident on the left side of the computational phantom.

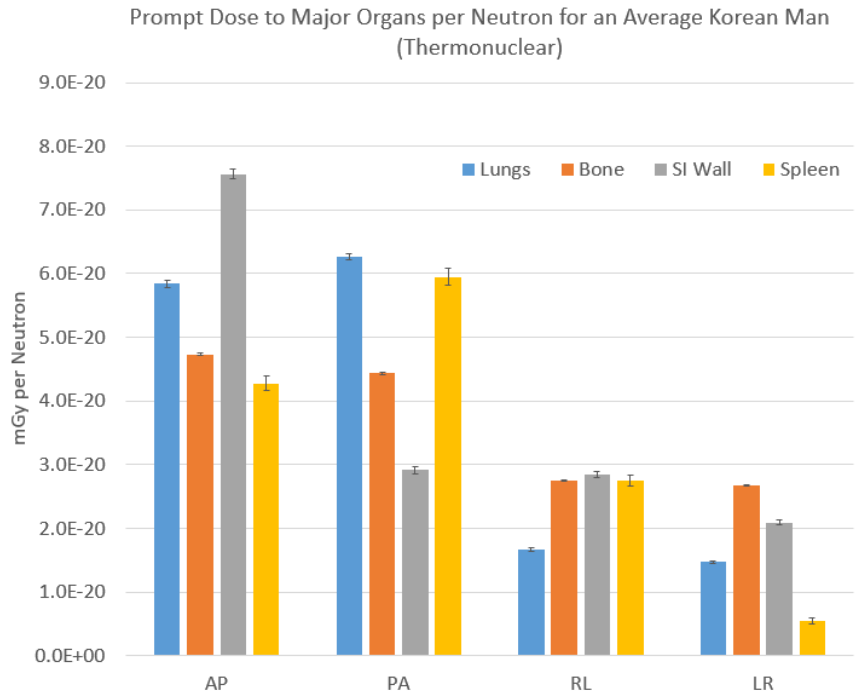

Figure 9. Prompt neutron dose to major organs from a low-yield thermonuclear detonation.

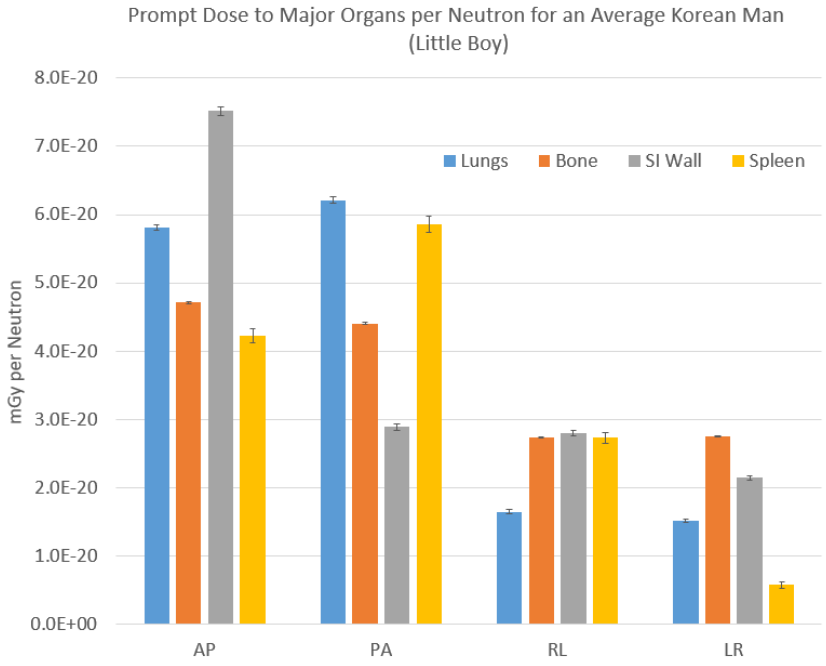

Figure 10. Prompt neutron dose to specific organs from a fission (Little Boy) detonation.

The following figures are shown as a means of understanding how the neutrons and secondary radiations interact within the computational phantom. Figure 11 is a representative depiction showing the depth of the flux density (ratio of the particle track length and the volume element in units of $1/cm^2$) colored in yellow with those areas where little neutron interaction occurred in blue.

Note that the yield is not the neutron yield of the weapon but the number of neutrons incident on the phantom.

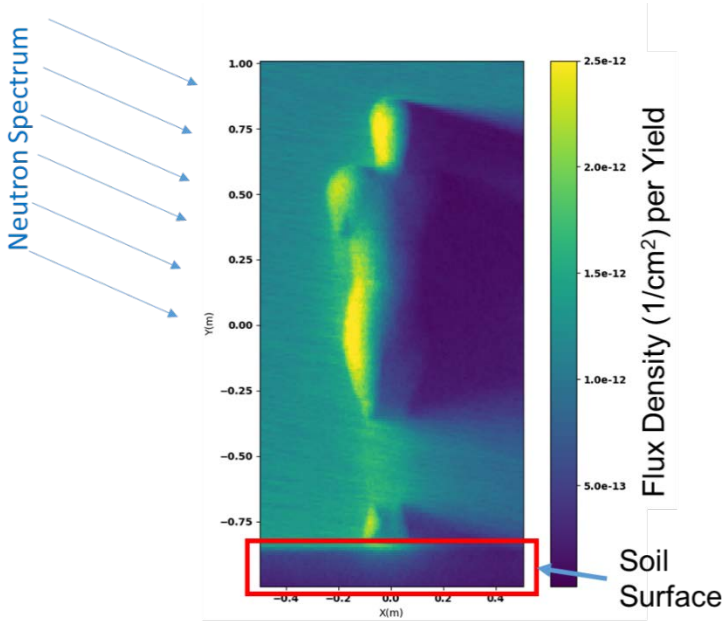

Figure 11. Representative example of the computational phantom on soil with the neutron spectrum incident on the phantom's right lateral side.

The following figures show the radiation flux in the computational phantom from a thermonuclear spectrum incident on the phantom from the anterior to posterior, posterior to anterior, right lateral, and left lateral. The directional computations were performed for source neutrons greater than 1 MeV and less than 1 MeV. This energy separation was selected because protons have a very small mean free path in tissue when set in motion by source neutrons of energy less than 1 MeV.

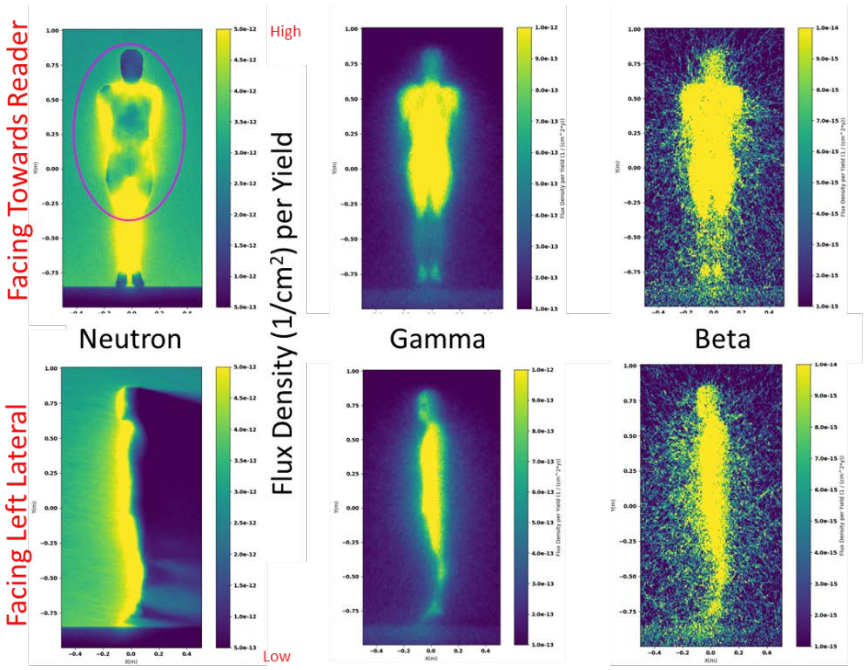

Figure 12. TN spectrum incident anterior to posterior on a computational phantom. The spectrum only shows those incident source neutrons of less than 1 MeV. Note the torso area experiences much less neutron radiation flux than the rest of the anterior portion of the body. The flux density effect probably results from the absorption of the majority of neutrons prior to the mid line of the torso.

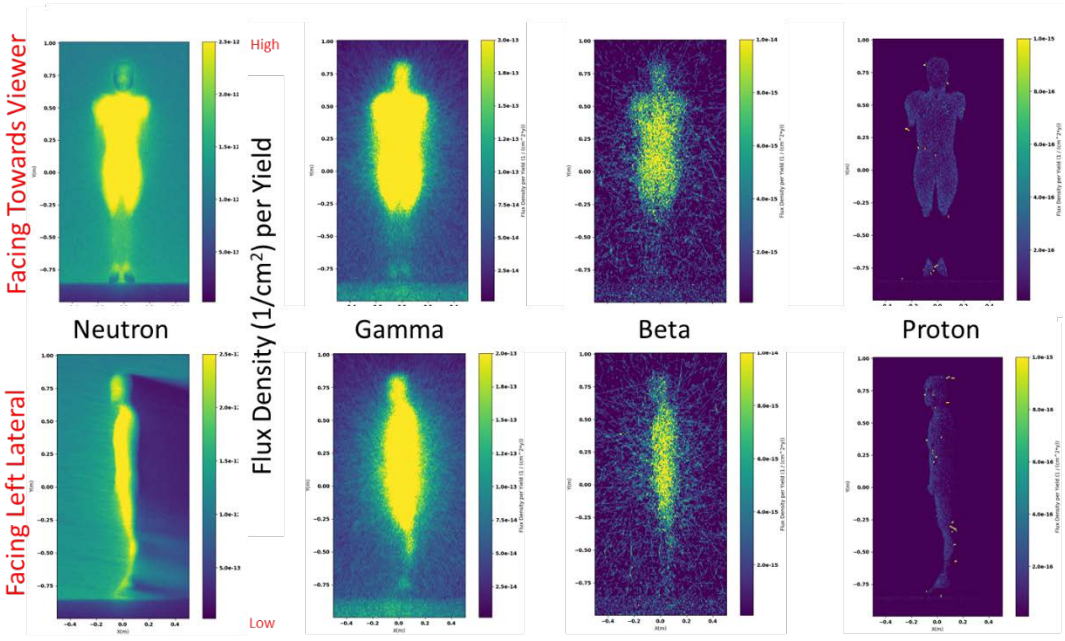

Figure 13. TN spectrum incident anterior to posterior on a computational phantom. The spectrum only shows those incident source neutrons of greater than 1 MeV.

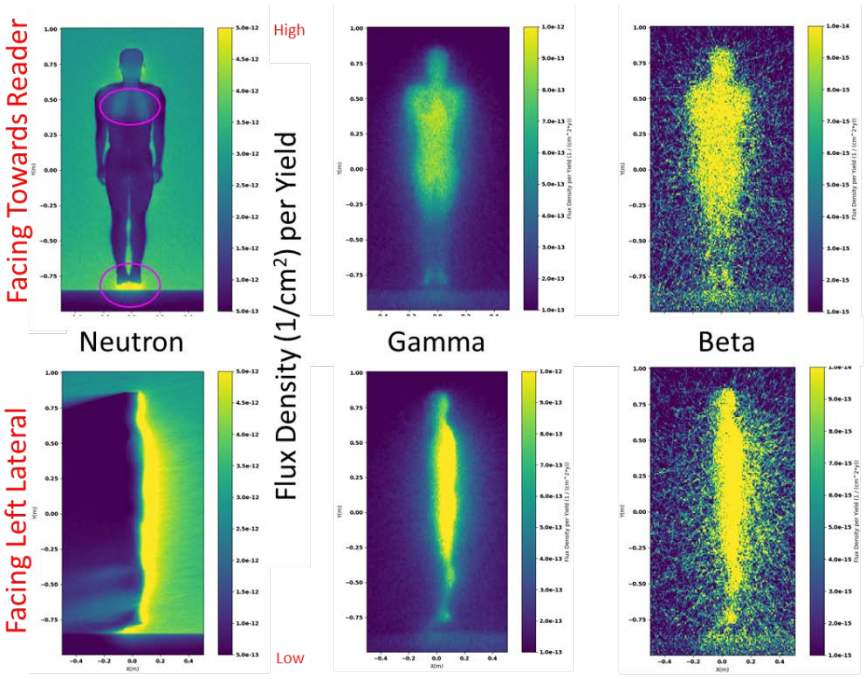

Figure 14. TN spectrum incident posterior to anterior on a computational phantom. The spectrum only shows those incident source neutrons of less than 1 MeV. Note the neutron radiation flux in the lungs and at the feet. The radiation flux at the feet is a result of the phantom standing on its toes.

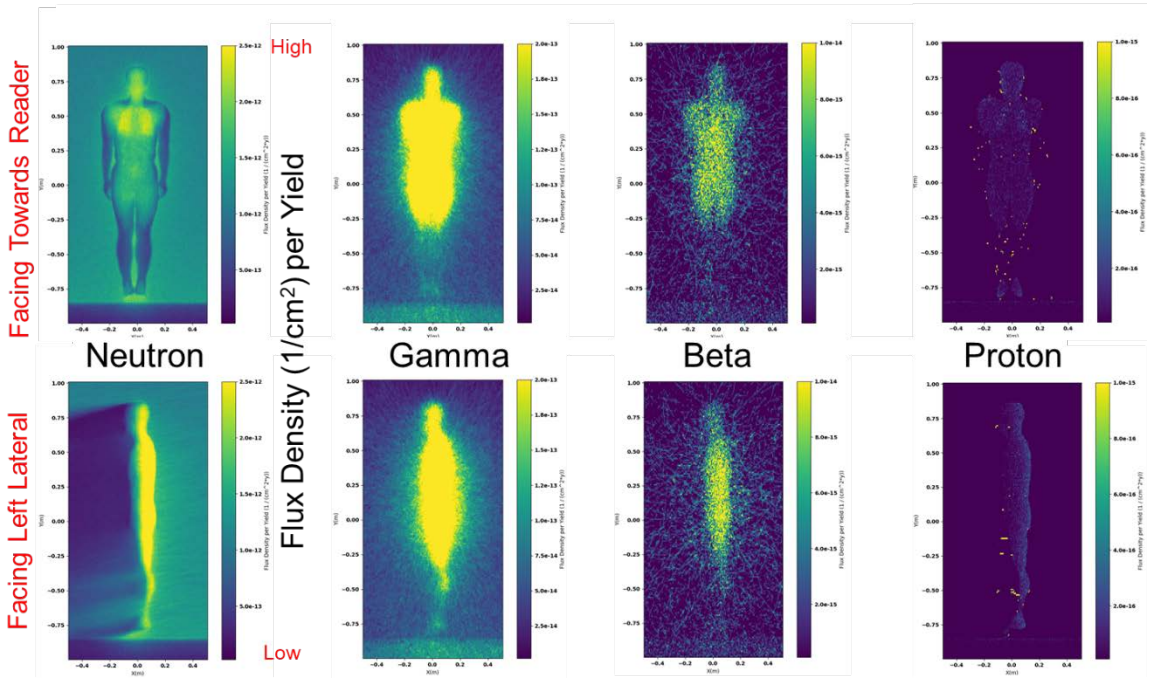

Figure 15. TN spectrum incident posterior to anterior on a computational phantom. The spectrum only shows those incident source neutrons of greater than 1 MeV.

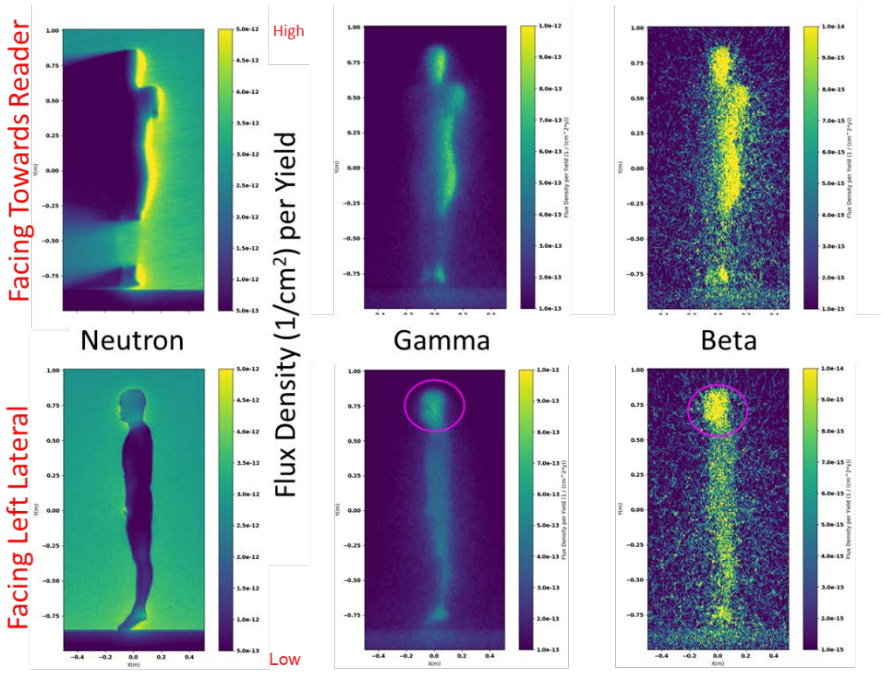

Figure 16. TN spectrum incident left lateral on a computational phantom. The spectrum only shows those incident source neutrons of less than 1 MeV. Note the higher radiation flux density in the head from the gamma and beta radiation.

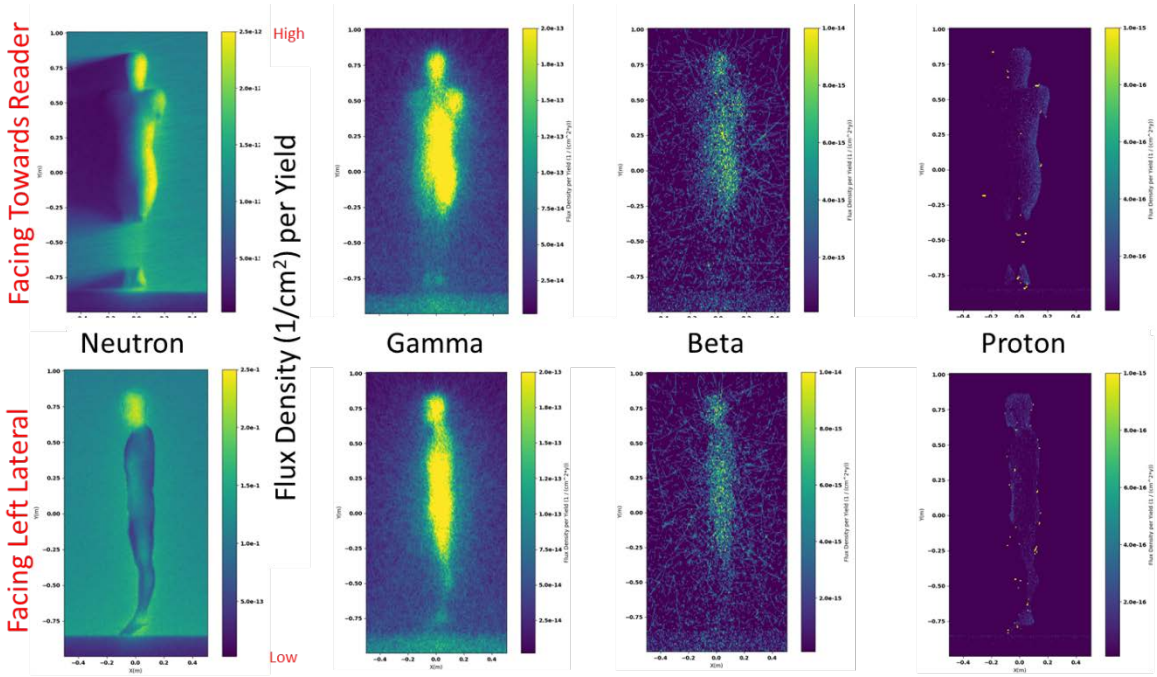

Figure 17. TN spectrum incident left lateral on a computational phantom. The spectrum only shows those incident source neutrons of greater than 1 MeV.

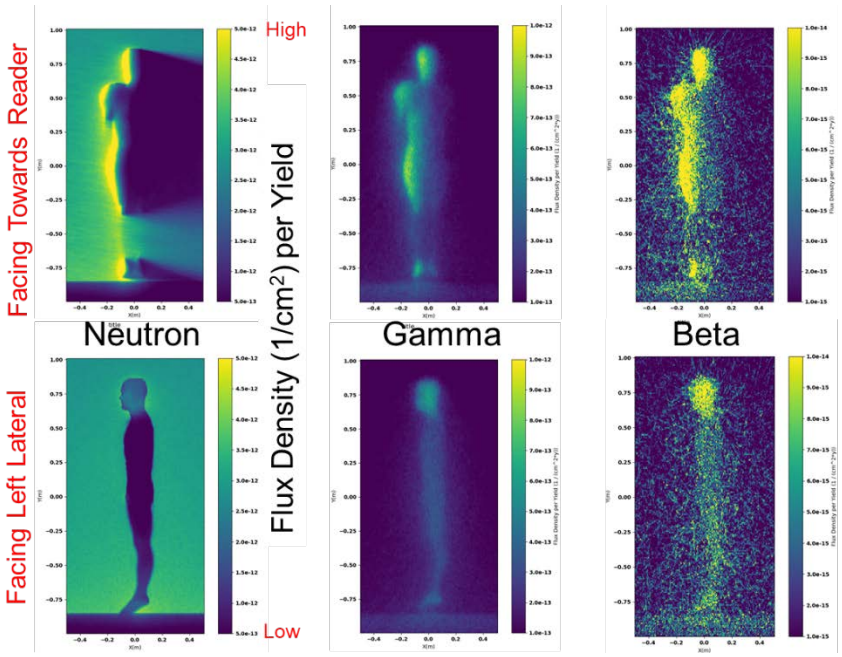

Figure 18. TN spectrum incident right lateral on a computational phantom. The spectrum only shows those incident source neutrons of less than 1 MeV.

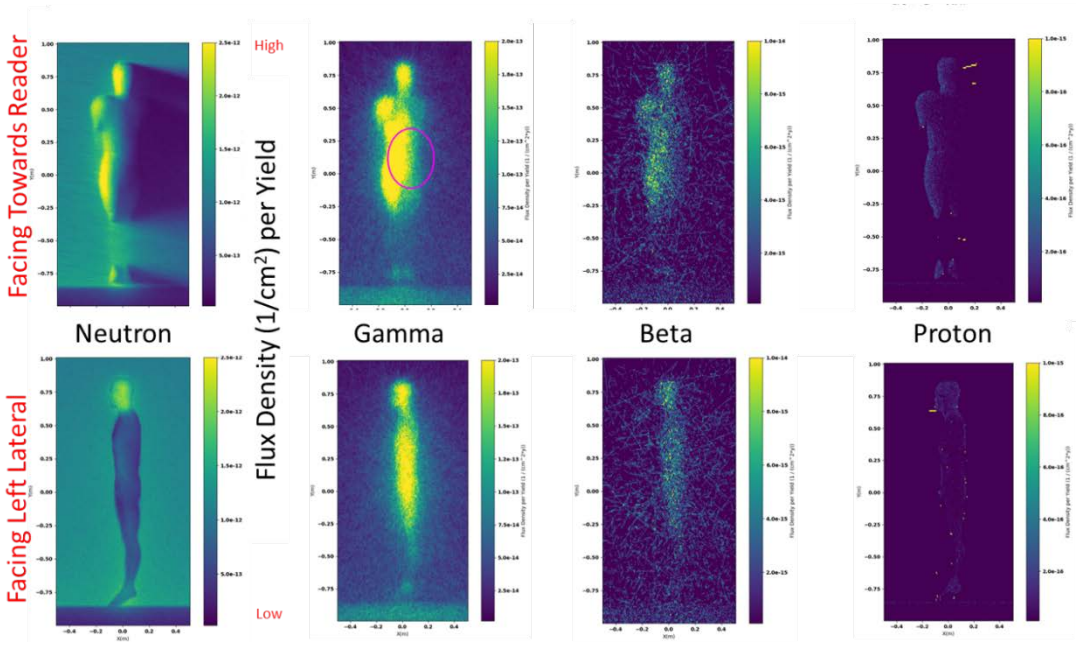

Figure 19. TN spectrum incident right lateral on a computational phantom. The spectrum only shows those incident source neutrons of greater than 1 MeV. Note the gamma dose sparing that occurs on the distal side.

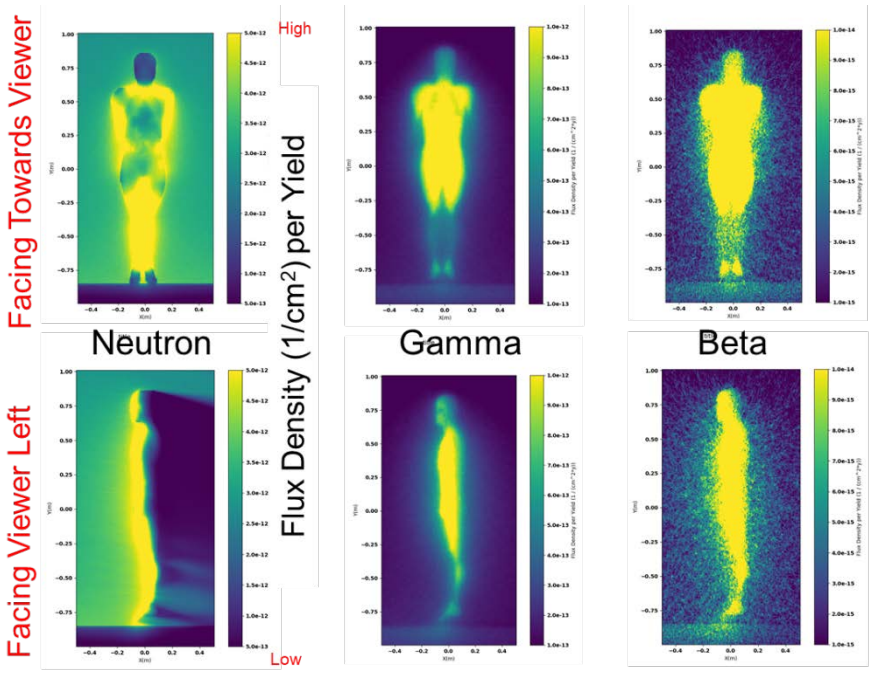

Figure 20. LB spectrum incident anterior to posterior on a computational phantom. The spectrum only shows those incident source neutrons of less than 1 MeV.

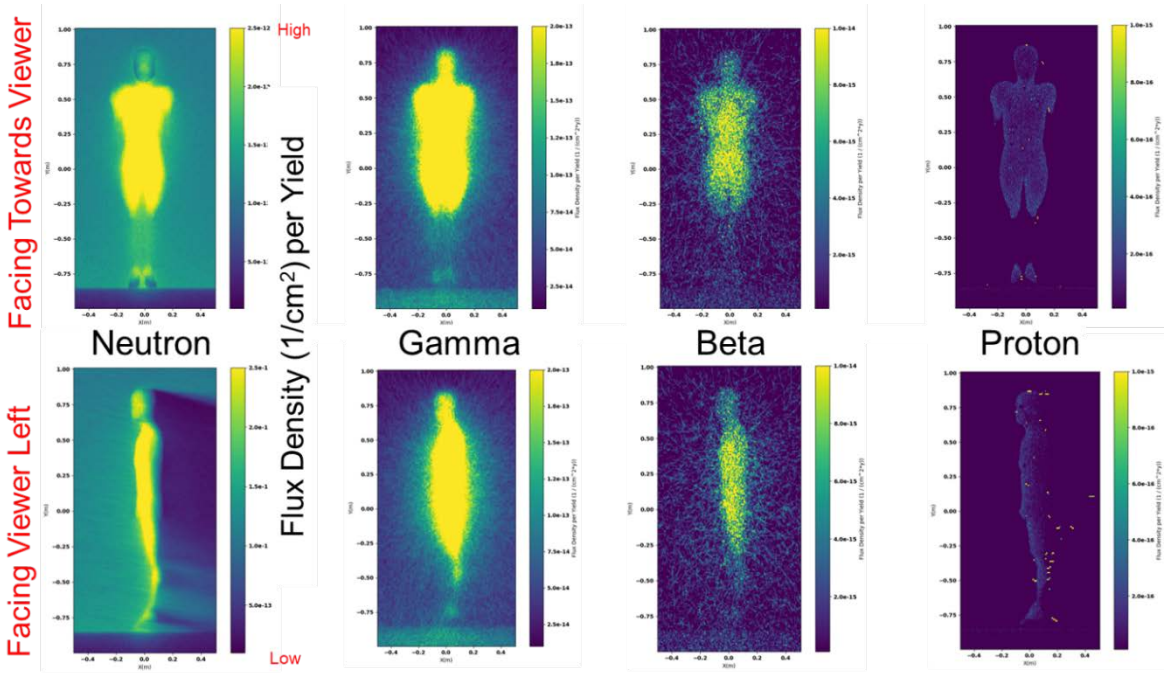

Figure 21. LB spectrum incident anterior to posterior on a computational phantom. The spectrum only shows those incident source neutrons of greater than 1 MeV.

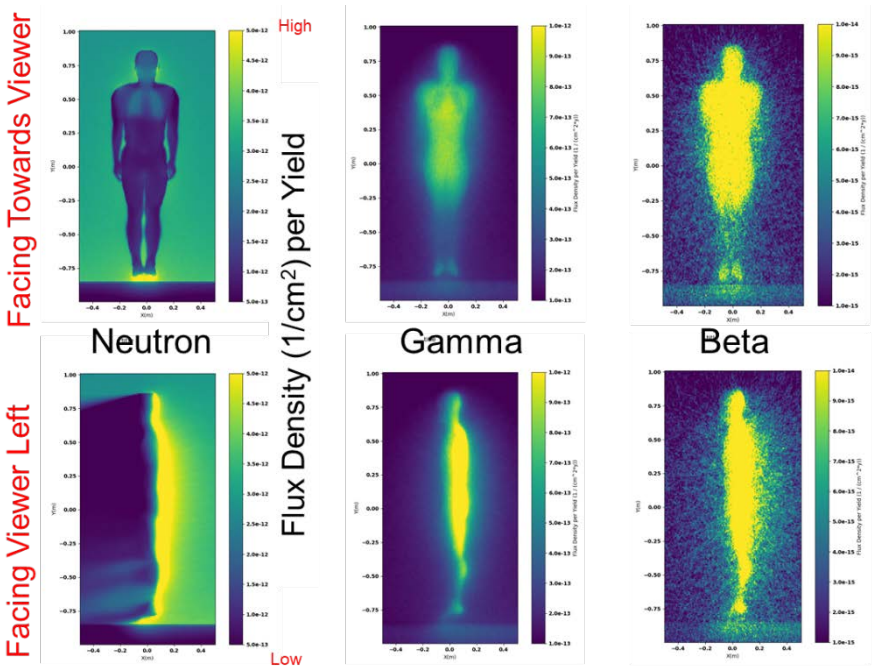

Figure 22. LB spectrum incident posterior to anterior on a computational phantom. The spectrum only shows those incident source neutrons of less than 1 MeV.

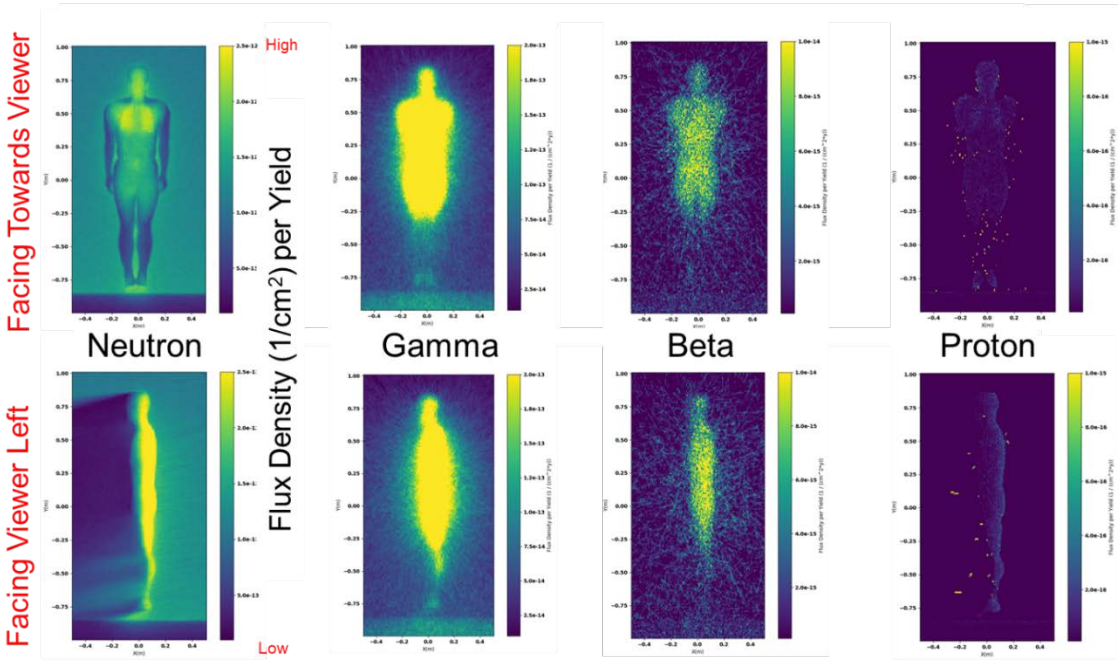

Figure 23. LB spectrum incident posterior to anterior on a computational phantom. The spectrum only shows those incident source neutrons of greater than 1 MeV.

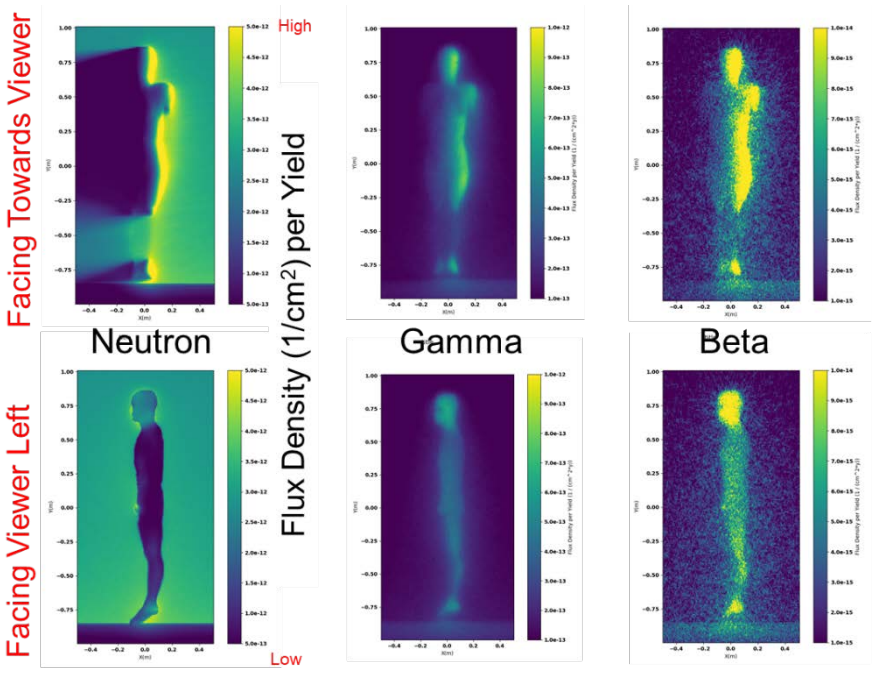

Figure 24. LB spectrum incident on the left lateral side of a computational phantom. The spectrum only shows those incident source neutrons of less than 1 MeV.

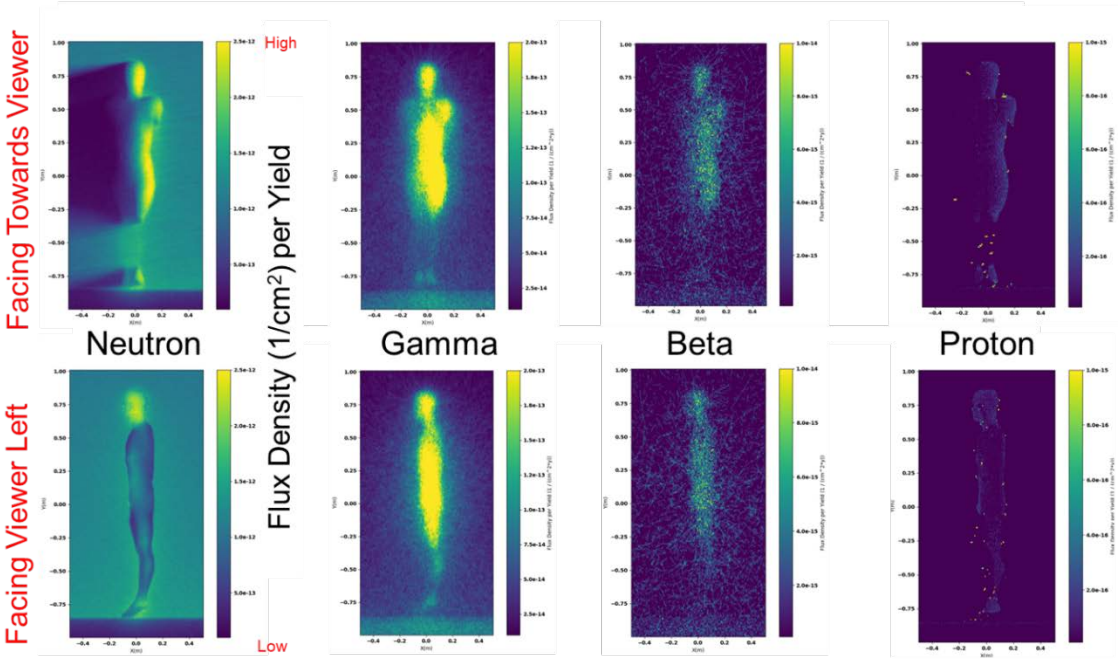

Figure 25. LB spectrum incident on the left lateral side of a computational phantom. The spectrum only shows those incident source neutrons of greater than 1 MeV.

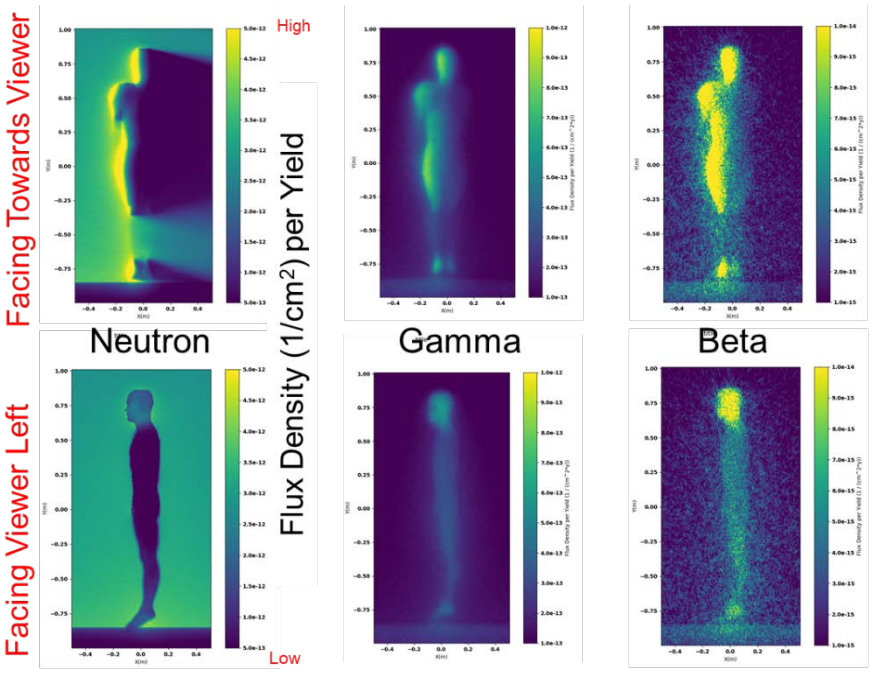

Figure 26. LB spectrum incident on the right lateral side of a computational phantom. The spectrum only shows those incident source neutrons of less than 1 MeV.

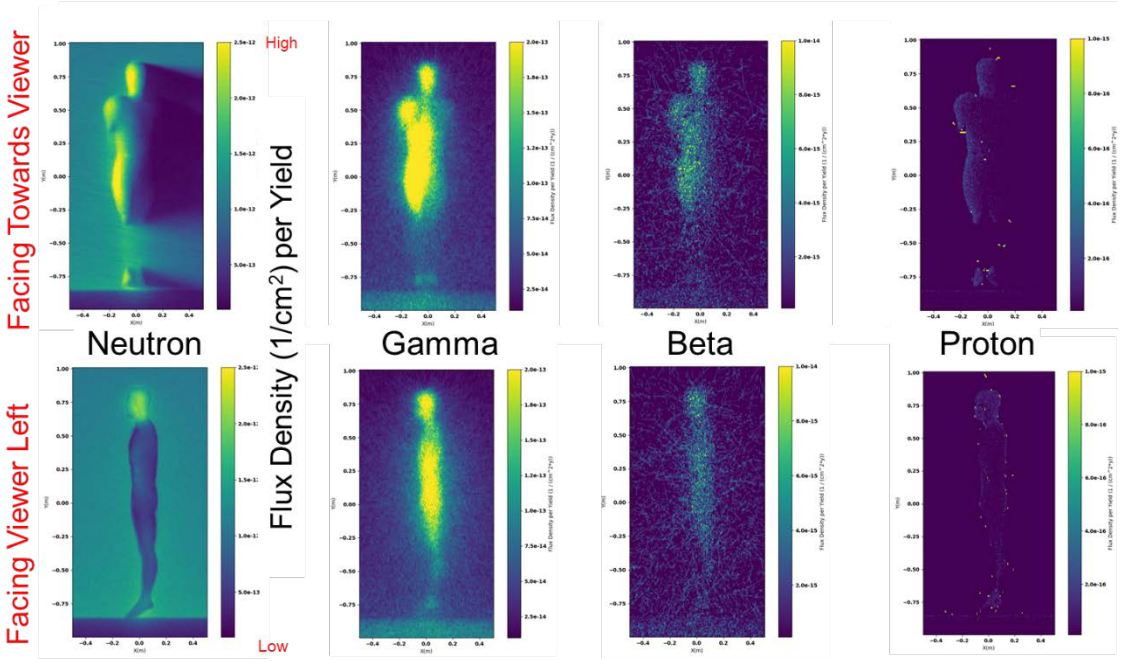

Figure 27. LB spectrum incident on the right lateral side of a computational phantom. The spectrum only shows those incident source neutrons of greater than 1 MeV.

Section 4. Discussion

The released neutrons from the source material in a NUDET will either contribute to the chain reaction needed to continue the fission or fusion reactions or will escape from the exploding fuel and weapon casing. The different factors contributing to the total neutron energy include the type of weapon, the fraction of energy released from the fission or fusion reactions, and the material surrounding the weapon. The escaped neutrons will subsequently interact with the surrounding environment and will continue to experience scattering events until absorption, with the absorption cross section increasing as energy decreases.

The computation model does not necessarily follow the neutron and associated daughter products through all interactions. In fact, if the neutron liberates a gamma or an electron from its surrounding and that daughter drops below a threshold energy (1 keV) any point during its history then its history is killed and its remaining energy is deposited thermally in the present cell. In principal, neutrons have no such cut-off energy and can propagate for much longer, but in practice as they become increasingly thermal the absorption cross section increases dramatically. Finally, if the MCNP weight function (analogous to the quantum wave function amplitude) drops below a threshold, there is a chance any particle will be spontaneously discarded.

For thermal and epithermal neutron energies, secondary photons emitted from the neutron capture by hydrogen and the subsequent photon interactions (i.e. electrons and positrons) account for the major fraction of absorbed dose. The rest of the absorbed dose fraction comes from nitrogen capture and the resulting recoil proton. The recoil proton in a nitrogen capture reaction has an approximate energy of 580 keV plus the energy of the absorbed neutron and travels about 30 microns in tissue. Since there are about 41 times more hydrogen atoms than nitrogen atoms in tissue (muscle), thermal neutrons have a higher probability of interaction in tissue. As a result, the absorbed dose is primarily dominated by the hydrogen capture interaction with subsequent release of the photon. In the neutron energies above the epithermal range, elastic scattering with hydrogen dominates and the production of charged particles and their deposition physics becomes important (ICRP, 2010).

The neutron energy spectrum in the survivable zone ranges from thermal up to fast energies (in excess of 10 MeV). Scattering reactions will occur with all of the low atomic-number elements comprising the human body so a mixed-field spectrum of neutrons and photons will be established. The distance traveled in the body by a thermal or slow neutron will be small and, as a result, the regions where the energy was deposited by the neutron is near the surface of the body. These thermal and epithermal neutrons have a high probability of interacting with skin, fat, and muscle. The higher-energy neutrons will be less likely to experience absorption events near the surface of the body and will instead likely undergo more elastic and inelastic scattering events until the eventual absorption or capture at locations deeper in the body. In this fashion, fast neutrons have a higher probability of penetrating deeper in the body than thermal or epithermal neutrons. The neutron energy will be deposited heterogeneously throughout the body.

Dosimetry studies provide quantitative correlations between the amount of radiation absorbed by tissues and the biological effects resulting from the energy deposition. Absorbed dose averaged over an organ is a relevant quantity to relate the level of damage induced by the radiation depositing energy in the body to the incident radiation spectrum at a specific location away from ground zero. Although computational phantoms are limited by the resolution of the voxel structure, they can be powerful tools for understanding the deposition of energy from external and

internal radiation sources when combined with radiation transport programs (i.e. MCNP6.2). We specifically applied an external neutron source spectrum to be incident on the phantom. We then modeled the absorbed radiation dose deposited in different organs. The modeled dose considered the number of histories (particles), history weight fraction, energy deposited in the cell, average cell density, and the tally element volume. We used MCNP6.2 to define the energy deposited in the cell as that energy which does not go into the kinetic energy of a beta, gamma, neutron, or proton secondary radiation since those secondary radiations were tracked separately. Neutrons are not directly ionizing so subsequently the secondary radiations from a scattering or capture event will deposit almost all the total energy.

Organ absorbed dose systematic errors are chiefly a result of the computational phantom's low resolution. For example, complex tubular organ geometries (i.e. small intestines, respiratory and alimentary tracts) are difficult to model with voxel structures. Newer mesh-type computational phantoms are much better at modeling these types of rounded organs. In this study, the highest computational statistical error (measure of the precision of the estimated quantity), regardless of the direction of the incident spectra, was associated with the spleen. This statistical error is a result of the spleen being a much smaller geometric cross section organ than the other organs in the study. Although statistical error is already quite low, higher precision can be gained by using more particle histories and/or variance reduction techniques.

The organ tallies from MCNP have units of MeV per gram per neutron. For the convenience of the reader, we have converted these units to Gy per neutron. Since the simulation has already computed the energy deposited by neutrons in the body, further converting this value into a measurement which is dependent on the relative biological health effect for the source particle – such as Sieverts per neutron – would be redundant.

In order to understand the absorbed dose to the specific organs, the number of neutrons impinging on the phantom must be estimated. Estimating the total number of neutrons at a location in an urban environment was beyond the scope of this research as we were more interested in the neutron and secondary radiation energy deposition in specific organs. However, in a doctoral dissertation researching thin lithium ion batteries, Zhang simulated the Little Boy neutron spectrum at 1,000 m (non-urban environment moderate damage zone, 800 m to 1,500 m) from ground zero (Zhang, 2017). Zhang estimated the Little Boy neutron fluence, Φ, at a point as

$$\Phi\left(\frac{n}{cm^2}\right) = \frac{\left(5.42x10^{23}\left(\frac{n}{kT}\right)\right)Y}{r^2} e^{\left(\frac{-\rho r}{1.79x10^4\left(g*\frac{cm}{L}\right)}\right)}, \quad (1)$$

where Y is the weapon yield (approximately 10 kT for the Little Boy NUDET), r is the radial distance from the point of detonation in cm (1.5 x 10^5 cm – to be consistent with Zhang), and rho (ρ) is the air density (~1.29 g/L on an average clear day at sea level, zero degrees Celsius, and average barometric pressure). We computed the absorbed dose received by a specific organ by multiplying the absorbed dose per neutron value (G) presented in Table 4, Table 5, Table 6, and Table 7 by the total number of prompt neutrons which survive to the relevant distance. For example, consider the total radiation dose to the lungs during an anterior-posterior exposure using the Little Boy NUDET at 1.5 km. The LB absorbed dose to the lungs per neutron, G, can be found in Table 6 with the result being 5.81E-20 mGy/n. The number of neutrons can be found by determining the fluence (Eq 1) integrated over a surface which is equal to the radial distance of the simulated area. Since it would be inconvenient for our G value to depend on the size of the

simulated area (which was an arbitrary choice), we have normalized all values in tables 4, 5, 6, and 7 to a sphere with a size of 1.5 km.

Therefore, to compute N,

$$N \approx \iint_{\theta,\varphi}^{Sphere} \Phi\left(\frac{n}{cm^2}\right) \cdot dA = \Phi * A, \quad (2)$$

where we assume an isotropic neutron distribution over the surface of the sphere. Therefore, the dose for a given organ is:

$$\text{Dose(Gy)} = \text{N}[n] * \text{G}\frac{[mGy]}{[n]} = \Phi\frac{[n]}{[cm]^2} * 4\pi r^2[cm]^2 \ * G\frac{[mGy]}{[n]} \quad (3)$$

Combining these inferences we estimate the total dose received by our four organs of interest for an Average Korean Man in an urban environment and on a clear, cool day at a distance of 1.5 km from the detonation vertex of a 10 kT Little Boy-like NUDET. Our resulting estimations are given in Table 8 and the accompanying statistical error is given in Table 9 (systematic error is not estimated).

Table 8. Estimated prompt neutron dose to several major organs in the Little Boy NUDET on an average Korean man at a distance of 1.5 km for four different facings. Estimation merges the Monte Carlo presented in this paper with theoretical predictions in Zhang.

Little Boy Neutron Dose at 1.5 km (Estimate)				
(mGy)	Lung	Bone	SI Wall	Spleen
AP	29.9	24.3	38.8	21.8
PA	32.0	22.7	14.9	30.2
RLat	8.5	14.1	14.4	14.1
LLat	7.8	14.2	11.0	3.0

Table 9. Associated statistical error for dose estimations provided in Table 8. Systematic error is not estimated.

Statistical Error				
(mGy)	Lung (%)	Bone (%)	SI Wall (%)	Spleen (%)
AP	0.234	0.068	0.329	0.538
PA	0.242	0.066	0.232	0.619
RLat	0.129	0.053	0.208	0.427
LLat	0.125	0.053	0.183	0.249

We provide these results as an example for estimated application of the results presented in the previous sections. To compute the estimated organ dose at an arbitrary distance for an arbitrary weapon design, additional information – such as that provided in the Zhang (Zhang, 2017) – is required.

The reader will recall, that although we provide a method of estimating the effective neutron dose here, gammas and other secondary photons will contribute the majority of the absorbed dose in the body. If all radiative particles had the same relative biological effectiveness (RBE), then estimating the overall absorbed dose would be relatively easy. However, radiative particles do not have the same RBE. Neutron RBE will be larger at low dose rate than for an acute exposure, since

the effectiveness of neutrons decreases with dose rate to a much smaller extent than is the case for x- or gamma-rays (Hall, 2000). In this manner, a low-energy neutron, often reduced to this energy by numerous interactions (elastic and inelastic scattering), can be more damaging to human tissue than an x- or gamma-ray.

The neutron RBE values for deterministic effects (RBE_m) vary among the different organs (ICRP, 1990). For early damage, the RBE_m for the lung is between 6 and 7. Neutron RBE_m values for the hematopoietic system have been derived from spleen colony stem cell survival curves and range from 1.9 to 4 for fission neutron doses of 7- and 2-Gy respectively. Similarly the neutron RBE_m values for the gastrointestinal tract range from 3 to 4 for 14 MeV neutrons to 7 for 7.5 MeV neutrons.

The spectra used in this study are different than the experimental spectra used in ICRP Publication 58 studies. The spectra in our research was propagated in an urban environment and can also provide additional insights into how neutrons behave in a surrogate human body. By separating the NUDET mixed radiation spectrum at a location into separate gamma-ray and neutron spectra, the specific absorbed dose ratios (e.g. neutron absorbed dose to the total absorbed dose) can be calculated. These calculated ratios can then be used with ICRP Publication 58 formulae to calculate the RBE of the mixed radiation spectrum.

Section 5. Conclusions

The majority of neutrons emitted in a nuclear weapon spectrum are at the low energies. Since the low-energy neutrons have a higher probability of interacting with the surrounding media, these neutrons will tend to deposit their energy closer to the detonation and not reach the forward edge of the survivable zone. The high-energy neutrons, however, will likely travel further through the environment and deposit their energies at greater distances, including into the survivable zone where personnel will survive the prompt effects but absorb radiation dose from the prompt neutrons and gammas. Neutrons have higher probability of inelastic scattering and absorption with elements with a low atomic number. Since the human body is primarily made up of low atomic number elements, the deposition of neutron energy will result from the inelastic scattering and absorption interactions.

We conducted the dosimetry study of four different organs systems that are important indicators in how the body either fights infection, absorbs nutrients into the blood stream, or experiences an inflammatory response to large amounts of absorbed radiation. Acute radiation syndrome is primarily a result of the amount of gamma radiation that has been absorbed in the human body. However, even though less neutron energy is deposited in the human body in a survivable zone than the amount of energy deposited by gammas, the neutron dose should not be considered as negligible. Prior research has shown that the survivable radiation region for humans may not be as far away from the detonation location as previously thought. Assigning a whole-body dose to individuals in the survivable zone may not fully describe the deposition of the energy in the body to specific organs. Since medical countermeasures and prophylaxis are administered for specific purposes, knowledge of how the neutron energy is deposited can enable better medical treatments. Therefore, the acute health effects from the prompt neutron dose to personnel in the survivable range from a NUDET should be a planning consideration for medical planners and health practitioners.

Section 6. Future Direction

Traditionally, the common practice for acute exposures has been to sum the neutron and gamma absorbed dose contributions and then apply an RBE value (normally a value of 1 is used for neutrons (Oxford, 2016)). The RBE of gamma rays is taken to be unity. As our research has shown, we have the computational ability to evaluate the absorbed dose in an organ system based upon an initial neutron spectrum. Using computational phantoms allows NUDET spectrum separation of neutrons and gamma-rays in a mixed-radiation field environment. Separating the incident spectrum is desirable as neutrons have a higher biological effectiveness per unit of absorbed dose than gamma-rays (Attix, 1986). While homogeneous tissue phantoms (e.g. water) are fine for gamma-ray dosimetry experiments, human-equivalent phantoms with specific tissue/organ compositions are needed for neutron dosimetry experiments. Computational phantoms can be appropriately designed with specific tissue compositions to conduct computational absorbed dose experiments with varying neutron spectra.

Our future efforts will address the urban environment in more detail by varying the distance from ground zero to the beginning of the urban potentially survivable radiation injury zones (550 m to about 800 m and 650 m to about 1,000 m for the Little Boy and Low Yield source term respectively (Kramer, 2018)) in order to better estimate the neutron and gamma contributions to the total dose for specific organs. We can then apply the ICRP 58 methodology to inform an estimate of the deterministic RBE.

These computational experiments can be used to update how neutrons are accommodated in DTRA's health effects from nuclear and radiological environments (HENRE) (Oldson, Bellman, Stricklin, Millage, & McClellan, 2017). Currently, HENRE uses radiation induced performance decrement (RIPD) to accommodate the prompt neutron doses in the exposure history but does not distinguish the dose of one neutron spectrum from that of another (Pellmar & Oldson, 2012). As we have shown in this report, there are differences in absorbed dose among tissues. This research can also support HENRE updates by conducting specific computational experiments where an environment is designed to determine partial body dose contributions due to partial shielding from surrounding infrastructure. Currently RIPD does not assume that secondary gamma rays are generated by neutron interactions in the shielding. The RIPD midline tissue dose does include kerma from both the attenuated neutron flux and the secondary gamma rays produced in the body by the neutrons but does not include kerma from the secondary gamma flux produced outside the body in the surrounding environment. We can use computational phantoms and environments with differing neutron spectra to either update or confirm this assumption. Future efforts will integrate the mixed radiation RBE formulae into HENRE.

Currently, the HENRE fatigability and weakness, lymphopoiesis, and upper gastrointestinal distress models have a neutron RBE set to one. We should continue our neutron spectra sensitivity analysis research within HENRE to determine the overall effects of raising the neutron RBE from one to a higher number within the previously mentioned models and the MarCell model (a mathematical model developed to predict the hematopoietic response to protracted or fractionated radiation exposures based on data with acute prompt doses) (Pellmar & Oldson, Mathematical Basis of MarCell, ARA/HS-TN-11-008-A, 2011). These models are important in calculating equivalent prompt dose and predicting casualties from a NUDET.

References

Armed Forces Special Weapons Project. (1953). *The Biological Effectiveness of Neutron Radiation from Nuclear Weapons (Operation SNAPPER Project 4.3).* Defense Nuclear Agency, Washington, D.C.

Attix, F. (1986). *Introduction to Radiological Physics and Radiation Dosimetry*. Canada: John Wiley and Sons, Inc.

Auxier, J., Burson, Z., French, R., Haywood, F., Mooney, L., & Stroker, E. (1972). *Nuclear Weapons Free-Field Environment Recommended for Initial Radiation Shield Calculations.*: Oak Ridge National Laboratories, Oak Ridge, Tennessee.

Bond, V., Carter, R., Reed, J., Hechter, H., & Veenstra, R. (1953). *Biological Effectiveness of Ionizing Radiation within Shelters (Operation UPSHOT-KNOTHOLE Project 23.1).* U.S. Naval Radiological Defense Laboratory, San Francisco, CA.

Carter, R., Bond, V., Veenstra, R., Reed, J., & Silvia, P. (1953). *The Biological Effects of Neutrons (Operation UPSHOT-KNOTHOLE Project 4.8).* U.S. Naval Radiological Defense Laboratory, San Francisco, CA.

Cross Section Evaluation Working Group. (2018, December 28). *ENDF: Evaluated Nuclear Data File*. Retrieved from IAEA: https://www-nds.iaea.org/exfor/endf.htm.

Eldridge MD, L. (2019, February 18). *An Overview of Radiation Pneumonitis*. Retrieved from verywellhealth: https://www.verywellhealth.com/radiation-pneumonitis-symptoms-and-treatment-2249341.

Eldridge MD, L. (2019, February 18). *Types and Function of White Blood Cells (WBCs)*. Retrieved from verywellhealth: https://www.verywellhealth.com/understanding-white-blood-cells-and-counts-2249217.

Hall, E. (2000). *Radiobiology for the Radiologist. 5th Edition.* Lippincott Williams and Wilkins, Philadelphia, PA.

ICRP. (1990). RBE for Deterministic Effects. ICRP Publication 58. *Annals of the ICRP 20 (4)*.

ICRP. (2009). Adult Reference Computational Phantoms. ICRP Publication 110. *Annals of the ICRP 39 (2)*.

ICRP. (2010). Conversion Coefficients for Radiological Protection Quantities for External Radiation Exposures. ICRP Publication 116, *Annals of the ICRP 40(2-5).*

Kramer, K. (2018). *Urban Radiation Transport Studies on the Impact of Neutrons on Acute Radiation Injury Estimates,* ARA/HS-TN-18-007-A. Applied Research Associates, Inc., Arlington, VA.

Kramer, K., Dant, T., Li, A., & Millage, K. (2017). *Publicly Released Prompt Radiation Spectra Suitable for Nuclear Detonation Simulations, Revisions 1,* DTRA-TR-17-026 (R1). Defense Threat Reduction Agency, Fort Belvoir, VA; DTIC No. AD1044050.

Laboratory, B. N. (2005). *Evaluated Nuclear Data Files (ENDF): 293.6 Kelvin. ENDF/B-VII.0:x.* Brookehaven National Laboratory, Brookhaven, NY.

Mandal MD, A. (2019, February 18). *Function of the Spleen*. Retrieved from News Medical Life Sciences: https://www.news-medical.net/health/What-Does-the-Spleen-Do.aspx.

Mandal MD, A. (2019, February 18). *What Does the Small Intestine Do?* Retrieved from News Medical Life Sciences: https://www.news-medical.net/health/What-Does-the-Small-Intestine-Do.aspx.

McConn Jr, R., Gesh, C., Pagh, R., Rucker, R., & Williams III, R. (2011). *Compendium of Material Composition Data for Radiation Transport Modeling Revision 1, PIET-43741-TM-963 and PNNL-15870 Rev. 1.* U.S. Departments of Homeland Security and Energy, Washington, D.C.

McConn Jr., R., Gesh, C., Pagh, R., Rucker, R., & Williams III, R. (2011). *Compendium of Material Composition Data for Radiation Transport Modeling, Revision 1.* Radiation Portal Monitor Project. Pacific Northwest National Laboratory, Washington D.C.

Mickelson, A. (2012). *Medical Consequences of Radiological and Nuclear Weapons.* (A. Mickelson, Ed.). The Office of the Surgeon General, Falls Church, VA.

Oldson, D., Bellman, J., Stricklin, D., Millage, K., & McClellan, G. (2017). *(U) Henre 2.3 Technical Reference Manual,* DTRA-TR-15-071. Defense Threat Reduction Agency, Fort Belvoir, VA; DTIC No. AD1043149.

ORNL. (2019, February 25). *Radiation Safety Information Computational Center*. Retrieved from Oak Ridge National Laboratory: https://www.ornl.gov/division/rnsd/radiation-safety-information-computational-center.

ORNL. (2019, February 5). *Radiation Safety Information Computational Center*. Retrieved from Oak Ridge National Laboratory: https://www.ornl.gov/division/rnsd/radiation-safety-information-computational-center.

Oxford, S. M. (2016). *NATO Allied Medical Publication 7.5 (AMedP-7.5) NATO Planning GUide for the Estimation of CBRN Casualties Edition A, Version 1 Final Draft.* NATO Standardization Office. Institute for Defense Analysis, Alexandria, VA.

Pellmar, T., & Oldson, D. (2011). *Mathematical Basis of MarCell,* ARA/HS-TN-11-008-A. Applied Research Associates, Inc., Arlington, VA.

Pellmar, T., & Oldson, D. (2012). *Critical Review of Selected Components of RIPD (Radiation-Induced Performance Decrement),* DTRA-TR-12-047. Defense Threat Reduction Agency, Fort Belvoir, VA; DTIC No. ADA578704.

Pelowitz, D. (2011). *MCNPX Users Manual Version 2.7.0., LA-CP-11-00438.* Los Alamos National Laboratory, Los Alamos, NM.

Project, A. F. (1953). *Operation SNAPPER, Project 4.3 - The Biological Effectiveness of Neutron Radiation from Nuclear Weapons, Report WT-528.* Defense Nuclear Agency, Washington, D.C.

ScienceDaily. (2019, February 18). *ScienceDaily*. Retrieved from Bone Marrow: https://www.sciencedaily.com/terms/bone_marrow.htm.

Werner, C. (2017). *MCNP Users Manual - Code Version 6.2, Report LA-UR-17-29981.* Los Alamos National Laboratory, Los Alamos, NM.

X-5 Monte Carlo Team. (2008). *MCNP-A General Monte Carlo N-Particle Transport Code, Version 5 (LA-UR-03-1987).* Los Alamos National Laboratory, Los Alamos, NM.

Young, R., & Kerr, G. (2005). *Reassessment of the Atomic Bomb Radiation Dosimetry for Hiroshima and Nagasaki-Dosimetry Systems 2002.* Radiation Effects Research Foundation. Hiroshima, Japan.

Zhang, T. (2017). *Nuclear Fission Weapon Yield, Type, and Neutron Spectrum Determination Using Thin Li-ion Batteries.* Retrieved from Arizona State University: https://repository.asu.edu/attachments/186480/content/Zhang_asu_0010E_17010.pdf.

Abbreviations and Acronyms

AFRRI	Armed Forces Radiobiology Research Institute
ARA	Applied Research Associates, Inc.
C	Carbon
CPE	Charged particle equilibrium
DNA	Deoxyribonucleic acid
DoD	Department of Defense
DTRA	Defense Threat Reduction Agency
ENDF	Evaluated Nuclear Data File
GI	Gastrointestinal
H	Hydrogen
ICRP	International Commission on Radiological Protection
IND	Improvised Nuclear Device
ISO	Isometric
KTMan-2	Korean Typical MAN-2
LB	Little Boy
MCNP	Monte Carlo N-Particle
MCNPX	Monte Carlo N-Particle Version X
MCNP6.2	Monte Carlo N-Particle Version 6.2
MeV	Mega electron volt
N	Nitrogen
NUDET	Nuclear detonation
O	Oxygen
RBE	Relative biological effectiveness
RSICC	Radiation Safety Information Computational Center
TN	Thermonuclear
USANCA	US Army Nuclear and Countering Weapons of Mass Destruction Agency
WBC	White blood cells